

Chemical abundance analysis of symbiotic giants. Metallicity and CNO abundance patterns in 14 northern S-type systems

Cezary Gałań,^{1*} Joanna Mikołajewska,¹ Kenneth H. Hinkle,² Richard R. Joyce²

¹*Nicolaus Copernicus Astronomical Center, Polish Academy of Sciences, Bartycka 18, PL-00-716 Warsaw, Poland*

²*NSF's National Optical-Infrared Astronomy Research Laboratory, 950 N. Cherry Ave., Tucson, AZ 85719, USA*

Accepted 2023 July 8. Received 2023 July 7; in original form 2022 May 9

ABSTRACT

In previous works, we computed abundances for the red giant in nearly four dozen S-type symbiotic systems (SySt). The abundances provide information about metallicity, evolutionary status, and possible memberships in Galactic stellar populations. Here, we extend our studies with a northern hemisphere sample of SySt. This northern sample is dominated by Galactic disc/halo objects, whereas our previous southern sample is heavily biased toward the bulge population. Spectrum synthesis of high-resolution ($R \sim 50\,000$), near-*IR* spectra using standard LTE analysis and atmospheric models have been used to measure abundances of CNO and elements around the iron peak (Fe, Ti, Ni, and Sc) in the atmospheres of the red giant component. The SySt sample shows generally slightly sub-solar metallicity, as expected for an older disc population, with a median at $[\text{Fe}/\text{H}] \sim -0.2$ dex. Enhanced ^{14}N , depleted ^{12}C , and decreased $^{12}\text{C}/^{13}\text{C}$ indicate that all these giants have experienced the first dredge-up. Comparison with theoretical predictions indicates that additional mixing processes had to occur to explain the observed C and N abundances. Relative O and Fe abundances agree with those represented by Galactic disc and bulge giant populations in the *APOGEE* data, with a few cases that can be attributed to membership in the extended thick-disc/halo. As an interesting byproduct of this study, we observed a blue-shifted additional component on the wings of absorption lines in the spectra of AG Peg which could be connected with accretion on to the hot component.

Key words: stars: abundances – stars: atmospheres – binaries: symbiotic – stars: evolution – stars: late-type.

1 INTRODUCTION

Stellar astrophysics is now able to provide a fairly complete picture of single star evolution. However, a number of unresolved issues remain concerning binary evolution, particularly with symbiotic stars (SySt). These systems are composed of strongly interacting stars at remarkably different stages of evolution: an evolved red giant (RG) donor (either a normal giant in S-type SySt, or a Mira variable embedded in an optically thick dust envelope in D-type SySt) which transfers material to a hot, luminous companion, typically a white dwarf (WD) but a main-sequence star with an accretion disc or neutron star is also suggested in some cases, surrounded by an ionized nebula. SySt represent the interacting binary systems with the longest orbital periods ($P_{\text{orb}} \sim$ years to centuries) with separations large enough to accommodate the RG branch (RGB) or asymptotic giant branch (AGB) stars. SySt offer insight into all interacting binaries that include evolved RGB/AGB stars and accreting WDs during any phase of their evolution (see Mikołajewska 2012; Munari 2019, for a recent reviews of SySt).

Since some of SySt contain a massive WD with a high accretion rate, they have been proposed as possible progenitors for type Ia supernovae (see e.g. Hachisu et al. 1999; Mikołajewska & Shara 2017; Liu et al. 2018). A review of the most promising SN Ia progenitors among SySt is presented in Mikołajewska (2013).

The mass exchange between the components of binary systems is critical in defining their evolution. The symbiotic giant can range from spectral type G to late M, with corresponding differences in binary separation and mass transfer. The symbiotic giants are losing matter at a rate ($\geq 10^{-7}\text{Myr}^{-1}$) which is systematically higher than for single field giants (see Mikołajewska et al. 2003b). A substantial part of this mass can be accreted on to the compact object from wind and/or via Roche lobe overflow (Mikołajewska 2012). When the system was formed, the current hot stellar remnant was the more massive component, which when passing through its RG stage transferred part of its mass to the main-sequence companion, that is currently RG. That mass transfer episode should have left traces in the RG chemical composition, and indeed such chemical pollution has been detected in some RG-WD binary systems (Smith & Lambert 1988). In SySt with circularized orbits characterized by periods shorter than $P_{\text{orb}} \approx 900$ days one can expect that in most of them the mass transfer must have taken place in the past (see Section 2 of Mikołajewska 2012).

To study the issues of binary interactions and evolution in SySt, as well as their population origin, the chemical composition of the symbiotic giant atmospheres provides additional insight. Useful diagnostics include abundances of some specific chemical elements; e.g. s-process elements produced during the AGB phase, CNO abundances which can provide information about evolutionary status, or α elements in relation to metallicity, which can inform about Galactic population membership. Our previous measurements and analyses

* E-mail: cgalan@camk.edu.pl (CG)

concerned 37 objects from the southern hemisphere (Gałan et al. 2016, 2017), and have been largely focused on the bulge population. In this paper, we present abundances of CNO and elements around the iron peak (Fe, Ti, Ni, and Sc) derived through the spectral synthesis of the high-resolution near-*IR* spectra for an additional sample of 14 RGs in S-type SySt located in the northern hemisphere. The northern sample is important as it is dominated by Galactic disc/halo objects, whereas the southern sample is heavily biased toward the bulge.

The order of the paper is as follows. The spectroscopic observations and reductions are presented in Section 2. In Section 3 we estimate the atmospheric parameters of symbiotic giants. The applied methods and finally calculated abundances are shown in Section 4. The discussion of the results and conclusions are presented in Section 5 with a comparison to abundances from the *APOGEE* mass survey and theoretical models.

2 OBSERVATIONS AND DATA REDUCTION

High-resolution ($R = \lambda/\Delta\lambda \sim 50\,000$, $S/N \sim 100$), near-*IR* spectra of the program stars were observed with the Phoenix cryogenic echelle spectrograph (see Hinkle et al. 1998, for a complete description) using the 4 m telescope at the Kitt Peak National Observatory. 14 SySt were observed during four nights spanning September 3 – 6, 2014. The journal of our spectroscopic observations is given in Table 1. Three narrow spectral intervals were covered. One *H*-band region (width of ~ 65 Å) at a mean wavelength close to 15635 Å, and two slightly wider regions (~ 100 Å) around 22275 Å, and 23635 Å, hereafter designated as *K*- and *K_r*-band spectra, respectively. In most cases, all three regions were explored; however, for the five objects T CrB, FG Ser, V443 Her, V1413 Aql, and CH Cyg only the *H*-band region was observed.

The spectra were extracted from the raw data and wavelength calibrated using standard reduction techniques (Joyce 1992). The left and right aperture data for each object were reduced separately and combined into a single spectrum. In line with common practice, the wavelength scales of all spectra were heliocentric corrected. Telluric lines were removed (except for the *H*-band region that is free of telluric features) by reference to a hot standard star, that was observed at approximately the same time. The Gaussian instrumental profile in all cases is ~ 6 km s⁻¹ full width at half-maximum (FWHM), corresponding to instrumental profiles of ~ 0.31 , 0.44 , and 0.47 Å in the case of the *H*-, *K*- and *K_r*-band spectra, respectively.

Example spectra of EG And in all three intervals are shown in Figs 1 – 3. *H*-band spectra contain relatively strong first overtone OH lines and a selection of neutral atomic lines from Fe I, Ti I, Ni I that are superimposed on background weaker second-overtone CO vibration-rotation lines and CN red system $\Delta\nu = -1$ CN lines. The *K*-band region contains moderately strong Ti I lines as well as a few other neutral atomic lines from Fe I and Sc I superimposed on weak CN molecular lines from the CN red system $\Delta\nu = -2$ transition. The molecular lines from these two regions were used to determine abundances of C, N, and O. The atomic lines were used to derive abundances of elements around the iron peak: Sc, Ti, Fe, Ni. The *K_r*-band interval is dominated by strong CO features that are heavily blended. These were used to measure the ¹²C/¹³C isotopic ratio.

Table 1. Journal of spectroscopic observations obtained at *H*- (~ 15600 Å), *K*- (~ 22300 Å), and *K_r*-band (~ 23600 Å) regions with Phoenix spectrograph during 4 nights (September 3–6, 2014). The order of targets is according to the increasing R.A. – here as well as later in the tables and in appendixes. Orbital phases have been calculated according to the referenced literature ephemeris. In the right columns are the values of rotational velocity measured from our spectra (see Section 2). The velocity unit is km s⁻¹. Rotational velocities have been obtained from the measurement of full width at half-maximum (FWHM) of band Ti I, Fe I, and Sc I absorption lines. The last column presents the value of rotational velocity obtained from the fit of synthetic spectra.

	Sp. reg. band	HJD(mid) -2456900	Phase ^a	$V_{rot} \sin i$	
				FWHM	fit
EG And	<i>H</i>	3.95295	0.843	–	4.9
	<i>K</i>	4.95454	0.845	5.5±1.1	5.85
	<i>K_r</i>	5.94766	0.847	–	5.4
AX Per	<i>H</i>	3.95620	0.709	–	8.2
	<i>K</i>	4.95957	0.710	9.1±1.0	9.3
	<i>K_r</i>	5.95981	0.712	–	8.8
T CrB	<i>H</i>	6.66832	–	–	7.1
FG Ser	<i>H</i>	3.74483	0.270	–	9.3
V443 Her	<i>H</i>	3.75275	0.189	–	5.1
V1413 Aql	<i>H</i>	3.76963	0.618	–	16.8
BF Cyg	<i>H</i>	3.80657	0.275	–	8.0
	<i>K</i>	6.82913	0.279	8.5±0.9	8.9
	<i>K_r</i>	5.83552	0.278	–	8.8
CH Cyg	<i>H</i>	3.84599	0.855	–	8.1
QW Sge	<i>H</i>	3.81973	–	–	7.2
	<i>K</i>	6.84208	–	8.4±1.1	8.6
	<i>K_r</i>	5.84895	–	–	8.1
CI Cyg	<i>H</i>	3.83156	–	–	11.5
	<i>K</i>	6.85385	–	12.3±0.4	12.8
	<i>K_r</i>	5.86198	–	–	12.2
PU Vul	<i>H</i>	3.83743	–	–	6.5
	<i>K</i>	6.85975	–	7.5±1.0	8.4
	<i>K_r</i>	5.86988	–	–	8.4
V1329 Cyg	<i>H</i>	3.91592	0.582	–	9.5
	<i>K</i>	4.92762	0.583	10.3±0.5	10.1
	<i>K_r</i>	5.92546	0.584	–	9.8
AG Peg	<i>H</i>	3.93592	–	–	7.9
	<i>K</i>	4.94291	–	8.2±1.1	10.0
	<i>K_r</i>	5.93767	–	–	9.7
Z And	<i>H</i>	3.93949	0.753	–	5.9
	<i>K</i>	4.94679	0.755	7.5±0.9	7.9
	<i>K_r</i>	5.94139	0.756	–	6.2

Notes. ^aOrbital phases are calculated from the following ephemerides: EG And 2450683.16 + 482.57×E (Kenyon & Garcia 2016); AX Per 2450963.8 + 682.1×E (Fekel et al. 2000b); FG Ser 2451031.4 + 633.5×E (Fekel et al. 2000b); V443 Her 2450197.3 + 599.4×E (Fekel et al. 2000b); V1413 Aql 2450567.11 + 433.47×E (Poyner 2012); BF Cyg 2451395.2 + 757.2×E (Fekel et al. 2001); CH Cyg 2446353 + 5689×E (Hinkle et al. 2009); V1329 Cyg 2451565.0 + 956.5×E (Fekel et al. 2001); Z And 2450260.2 + 759.0×E (Fekel et al. 2000b).]

3 RED GIANT PARAMETERS

Calculation of chemical composition requires the use of model atmospheres corresponding to specific parameters characterizing the physical conditions prevailing in stellar atmospheres. The most important are effective temperature (T_{eff}) and surface gravity ($\log g$). They are predominantly derived based on analysis of spectral features from neutral and ionized species, usually of Fe. Lines of ionized species are not common in the near-infrared (*IR*) and our spectra, covering narrow wavelength ranges, do not contain any lines from ionized elements. In addition, there are not enough unblended lines

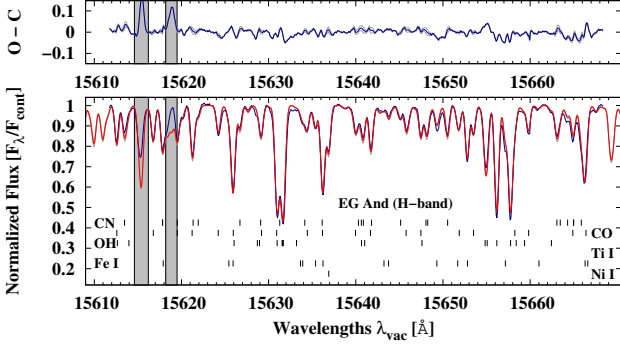


Figure 1. The H band spectrum of EG And (blue line) and a synthetic spectrum (red line) calculated using the final abundances (Table 4). The grey-shaded areas were excluded from calculations by a suitable mask.

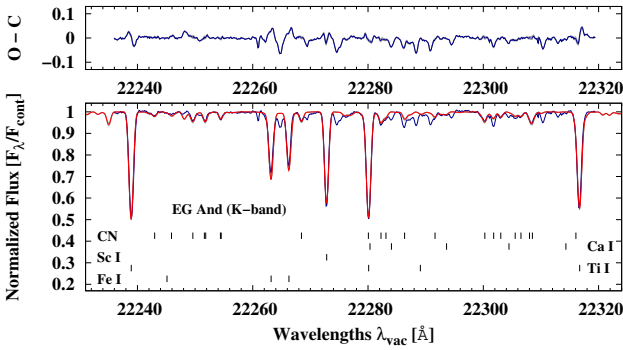


Figure 2. The K band spectrum of EG And (blue line) and a synthetic spectrum (red line) calculated using the final abundances (Table 4).

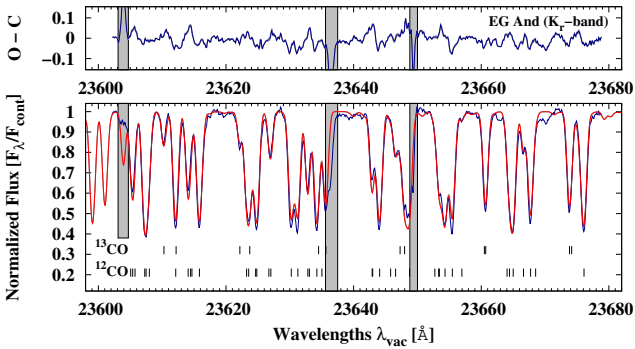


Figure 3. The K_r band spectrum of EG And (blue line) and a synthetic spectrum (red line) calculated using the final abundances (Table 4). The grey-shaded areas were excluded from calculations by a suitable mask.

with sufficiently different intensities for the same elements to be useful for determining these parameters. Therefore, we have deduced the stellar parameters using different methods and information available in the literature.

Estimation of T_{eff} was largely based on spectral types (Table 2) derived by Mürset & Schmid (1999) from analysis of TiO bands in the near- IR (I -band). However, in the case of AX Per, V1413 Aql, PU Vul, V1329 Cyg, and AG Peg we adopted slightly later spectral

types based on the spectra that were derived very close to inferior conjunction (RG component in front) or during mid-eclipses (see Belczyński et al. 2000, and references therein) and thus were less influenced by the hot companion. Calibrations by Richichi et al. (1999) and Van Belle et al. (1999) were used to translate the spectral types into T_{eff} . Independent estimation of an upper limit for temperature was derived from $J - K$ colours of Two Micron All Sky Survey (2MASS) photometry with the use of Kucinskas et al. (2005) $T_{\text{eff}} - \log g$ -colour relation for late-type giants gives generally consistent results (Table 2). The final values of T_{eff} adopted for further use are listed in the penultimate column of Table 2.

The majority of systems studied here are eclipsing binaries. In many cases, parameters of the RG are known (Table 3) from orbital analysis of both components (T CrB (Stanishev et al. 2004); AX Per (Mikołajewska & Kenyon 1992); BF Cyg (Fekel et al. 2001); V1329 Cyg (Fekel et al. 2001; Pribulla et al. 2003); AG Peg (Fekel et al. 2000a; Kenyon et al. 1993)) or at least of the RG component (EG And (Kenyon & Garcia 2016); FG Ser, V443 Her, Z And (Fekel et al. 2000b); CH Cyg (Hinkle et al. 2009)) and/or from analysis of ellipsoidal variability in light curves (EG And (Wilson & Vaccaro 1997); T CrB (Belczyński & Mikołajewska 1998); BF Cyg (Yudin et al. 2005a)). In two cases parameters derived from interferometric observations (FG Ser, AG Peg (Boffin et al. 2014)) were also used. This allows an estimate of the RG surface gravity (Table 3 and Table B2 – column (II)). In the absence of such information, the parameters were based solely on the Gaia (DR 3 and DR 2) parallaxes (Gaia Collaboration 2023, 2021, 2018) to estimate the RG’s radius (V1413 Aql and QW Sge). We relied on the *gofAL* (goodness-of-fit statistic parameter – see Table B1) to decide which measurement adopt as more reliable. Generally, in most cases, DR 3 gives a better fit but in two cases – V1413 Aql and BF Cyg – *gofAL* is much smaller in the case of DR 2, and in these cases, we adopted parallaxes from this previous release. However, it must be noted that in the cases of three targets (see Table B1) the *gofAL* is less than ~ 3 , which according to the Gaia documentation means the good fit to the data. Corresponding distances were taken as estimated with the dedicated special method by Bailer-Jones et al. (2018) which allows obtaining this information even with really bad quality measurements. Using known K_0 magnitudes and bolometric corrections (BC_K) by Bessell & Wood (1984) we estimated bolometric magnitudes (M_{Bol}) and luminosities to derive radii (Table B1) and finally calculate $\log g$. The H-R diagram for our sample compared to the *BaSTI evolutionary tracks* (Hidalgo et al. 2018) is shown in Figure A1 in Appendix A.

In cases when we have only spectroscopic orbit information we can use the RG velocity amplitude, K_g , and its rotational velocity, $V_{\text{rot}} \sin i$, in combination with Roche lobe geometry to estimate the minimum mass ratio q_{min} using the expression:

$$(1 + q)r(q) \geq \frac{V_{\text{rot}} \sin i}{K_g},$$

where the Roche limit (Eggleton 1983; Paczyński 1971):

$$r(q) = \frac{0.49q^{2/3}}{[0.6q^{2/3} + \ln(1+q^{1/3})]}$$

expresses the upper bound to the RG radius (R/a) to permit the system to remain detached. The known limit on the mass ratio enables us to estimate the minimal mass of the RG (M_g) through the known mass function and thus a lower limit to the surface gravity $\log g$ (Table B2 – column (I)) when the radius of the star is estimated from the known orbital period (P_{orb}), observed rotational velocity ($V_{\text{rot}} \sin i$), and inclination (i), and when the synchronous rotation with orbital motion is adopted. The obtained values can be verified

Table 2. Estimation of effective temperature T_{eff} and $\log g$ based on known spectral types and IR colours as well as the values adopted for this study.

	Sp.T. ^[1]	$T_{\text{eff}}^{[2]}$ [K]	$T_{\text{eff}}^{[3]}$ [K]	$J - K^{[4,5]}$ mag	$E(B - V)^{[6]}$ mag	$(J - K)_0$ mag	$T_{\text{eff}}^{[7]}$ [K]	$\log g^{[7]}$	T_{eff}^a [K]	$\log g^a$
EG And	M3	3560 ± 75	3586	~ 1.28	<0.07±0.01	~ 1.25	–	–	3600	0.5
AX Per	M6 ^b	3240 ± 75	3258	1.29±0.06	<0.19±0.01	>1.20±0.07	<3460±140	< 0.3 ± 0.2	3300	0.0
T CrB	M4.5	3410 ± 75	3421	1.23±0.05	<0.06±0.01	>1.20±0.06	<3460±120	< 0.3 ± 0.2	3400	0.5
FG Ser	M5	3355 ± 75	3367	1.56±0.07	<0.72±0.03	>1.20±0.10	<3450±210	< 0.3 ± 0.4	3400	0.5
V443 Her	M5.5	3300 ± 75	3312	1.32±0.07	<0.13±0.01	>1.26±0.07	<3340±150	< 0.1 ± 0.3	3300	0.5
V1413 Aql	M4.5 ^b	3410 ± 75	3421	1.27±0.06	<0.60±0.01	>0.98±0.07	<3940±160	< 1.2 ± 0.3	3400	0.5
BF Cyg	M5	3355 ± 75	3367	1.35±0.06	<0.24±0.01	>1.23±0.07	<3400±150	< 0.2 ± 0.3	3400	0.0
CH Cyg	M7	3100 ± 80	3149	~ 1.6	<0.07±0.01	~ 1.56	–	–	3100	0.0
QW Sge	M5	3355 ± 75	3367	1.39±0.08	<0.65±0.01	>1.07±0.09	<3730±190	< 0.8 ± 0.4	3400	0.5
CI Cyg	M5.5	3300 ± 75	3312	1.40±0.08	<0.44±0.03	>1.18±0.11	<3500±240	< 0.4 ± 0.4	3300	0.0
PU Vul	M6.5 ^b	3170 ± 75	3203	1.38±0.07	<0.29±0.01	>1.24±0.08	<3370±160	< 0.2 ± 0.3	3200	0.0
V1329 Cyg	M6.5 ^b	3170 ± 75	3203	1.46±0.06	<0.35±0.01	>1.29±0.07	<3280±140	< 0.0 ± 0.2	3200	0.0
AG Peg	M3.5 ^b	3510 ± 75	3531	1.19±0.06	<0.08±0.01	>1.15±0.07	<3570±140	< 0.5 ± 0.3	3500	0.5
Z And	M4.5	3410 ± 75	3421	1.34±0.06	<0.19±0.01	>1.25±0.07	<3360±140	< 0.1 ± 0.3	3400	0.5

References: spectral types are taken from ^[1]Mürset & Schmid (1999), total Galactic extinction adopted according to ^[6]Schlafly & Finkbeiner (2011) and Schlegel, Finkbeiner & Davis (1998), IR from 2MASS ^[4](Phillips 2007) transformed to ^[5]Bessell & Brett (1988) photometric system.

Calibration by: ^[2]Richichi et al. (1999), ^[3]Van Belle et al. (1999), ^[7]Kucinkas et al. (2005).

^a finally adopted to chose the *MARCS* model.

^b slightly later spectral types were adopted than those by Mürset & Schmid (1999) based on spectra obtained close to inferior conjunctions when they were not significantly influenced by nebulae (Belczyński et al. 2000).

Table 3. Estimated masses, radii, surface gravities, and orbital parameters of giants.

Object	M_g [M_{\odot}]	R_g [R_{\odot}]	$\log g$	P_{orb} [day]	K_g [km s^{-1}]	i [$^{\circ}$]
EG And	1.1–2.4 ^[1]	~ 110 ^a	0.4–0.7	482.6 ^[1]	7.34±0.07 ^[1]	70 ^[11]
AX Per	~ 1.0 ^[2,5]	132 ⁺²² ₋₂₂ ^a	0.05–0.35	682.1 ^[5]	7.81±0.21 ^[5]	70±3 ^[2]
T CrB	~ 0.9 ^[3,4]	~ 70 ^[3,4]	~ 0.7	227.6 ^[12]	23.89±0.17 ^[13]	60±5 ^[3]
FG Ser	1.7 ± 0.7 ^[5,6]	140 ⁺¹⁵ ₋₁₃ ^a	0.05–0.6	633.5 ^[5]	6.92±0.26 ^[5]	90 ^a
V443 Her	~ 2.5 ^[5,14]	166 ⁺²⁷ ₋₂₇ ^a	0.3–0.55	599.4 ^[5]	2.52±0.21 ^[5]	~30 ^[5,14]
V1413 Aql	1–2 ^b	147 ⁺⁷⁰ ₋₅₄ ^a	–0.2–0.8	433.5 ^[15]	–	–
BF Cyg	~ 2.2 ^a	≤ 240 ^a	≥ 0.0	757.2 ^[7]	6.72±0.24 ^[7]	~70–90 ^[7]
CH Cyg	~ 2.0 ^[9]	188 ± 44 ^[9]	0.0–0.4	5689 ^[9]	4.45±0.12 ^[9]	84 ^[9]
QW Sge	1–2 ^b	156 ⁺⁴² ₋₃₈ ^a	–0.15–0.6	390.5 ^[16]	–	–
CI Cyg	0.85–1.27 ^[17]	197 ⁺³⁷ ₋₃₇ ^a	–0.35–0.15	853.8 ^[13]	6.7±0.3 ^[13,17]	67–90 ^[18]
PU Vul	~ 0.8 ^[10]	187 ± 12 ^[10]	~ –0.2	4901 ^[20]	–	–
V1329 Cyg	2.02±0.51 ^[7,8]	195 ± 10 ^a	0.0–0.3	956.5 ^[19]	7.85±0.26 ^[7]	86±2 ^[19]
AG Peg	≥ 1.8 ^a	137 ± 11 ^a	≥ 0.35–0.5	818.2 ^[13]	5.44±0.20 ^[13]	90
Z And	~2 ^[5]	136 ⁺¹⁸ ₋₁₉ ^a	0.4–0.6	759.0 ^[5]	6.73±0.22 ^[5]	~ 60 ^a

References: ^[1]Kenyon & Garcia (2016); ^[2]Mikołajewska & Kenyon (1992); ^[3]Belczyński & Mikołajewska (1998); ^[4]Stanishev et al. (2004); ^[5]Fekel et al. (2000b); ^[6]Mürset et al. (2000); ^[7]Fekel et al. (2001); ^[8]Pribulla et al. (2003); ^[9]Hinkle et al. (2009); ^[10]Kato et al. (2012); ^[11]Wilson & Vaccaro (1997); ^[12]Kraft (1958); ^[13]Fekel et al. (2000a); ^[14]Dobrzycka et al. (1993); ^[15]Poyner (2012); ^[16]Munari & Jurdana-Šepić (2002); ^[17]Mikołajewska et al. (2006); ^[18]Kenyon et al. (1991); ^[19]Schild & Schmid (1997); ^[20]Cúneo et al. (2018).

^a adopted – see in the text (Appendix A).

^b the mass of RGs is unknown and it was adopted a typical mass of giant in the S-type SySt 1–2 M_{\odot} (Mikołajewska 2003).

using the aforementioned Kucinkas et al. (2005) calibration binding T_{eff} , $\log g$, and colour in a linear relation. However, a limitation of this approach is that the calibration is based on normal RGs, while symbiotic giants at least in some cases could turn out to be somewhat brighter luminosity class. Our previous results indicate that parameters of at least yellow SySt may need to be revised (Gałan et al. 2017). It is further supported by ellipsoidal light curves being discovered in more and more systems including roughly half of systems studied here (see discussion in Mikołajewska 2012, and Appendix A for individual cases) and the new Gaia distances which indicated

that giants in many of SySt must have significantly larger diameters, be significantly colder, and of higher luminosity class – bright giants rather than a normal giants. Furthermore, as we used the total Galactic extinction to de-redden IR colours, the obtained values (Table 2 and Table B2 – column (III)) should be treated as the upper limit to $\log g$ at least in the cases when the adopted $E(B - V)$ is large. The final adopted values of surface gravities are listed in the right-most column of Table B2 and are repeated in Table 2.

Additionally, the spectra contain wavelength shifts from radial velocity doppler effects and line broadening from stellar rotation as

well as small-scale micro- (ξ_t) and macro- (ζ_t) turbulence. ξ_t and ζ_t were set in our calculations to typical values for cool Galactic RGs, 2 and 3 km s⁻¹, respectively. Corrections for the velocity shifts (contributed mainly by radial velocities) were performed with the use of the values obtained through the fit of the synthetic spectra to the observed ones, during the initial phase of estimating the input parameters, which were then set as the fixed values during subsequent more accurate calculations of the chemical composition. In our spectra of giant stars with relatively narrow absorption features the largest contribution to the broadening of the spectral lines comes from the rotational velocity of the star ($V_{\text{rot}} \sin i$). We measured these values by adjusting them as free parameters in the course of the fitting with the synthetic spectra. In the case of the K -band spectra, we were also able to measure values of the rotational velocity directly from the full width at half-maximum (FWHM) of the six relatively strong unblended atomic lines (Ti I, Fe I, Sc I). The values obtained with both methods are generally in very good agreement (Table 1), except the case of AG Peg, in which the value derived from the synthetic fit is somewhat overestimated, due to the influence of an additional absorption component present in the line profiles (see Section 4 for more details).

4 ANALYSIS AND RESULTS

Elemental abundances were measured using the spectrum synthesis code (*WIDMO*; Schmidt et al. 2006) which applies local thermodynamic equilibrium analysis based on 1D hydrostatic model atmospheres (*MARCS*; Gustafsson et al. 2008). All details of our methods are described by Galan et al. (2016, 2017). The lists of the atomic and molecular lines with the excitation potentials and gf -values for transitions are the same as in our previous studies of symbiotic giants. For the H -band region, the atomic data are from the list by Mélandez & Barbuy (1999). For K - and K_r -band regions the lists from the Vienna Atomic Line Data base (Kupka et al. 1999) were used. For the molecular data, we used line lists by Goorvitch (1994) for CO, by Kurucz (1999) for OH, and by Sneden et al. (2014) for CN.

In summary, the abundance calculations were performed as follows. We sampled a number of *MARCS* models around those with the adopted best values of T_{eff} , $\log g$, and ξ , testing various metallicities and differently CN-cycled models as reflected in the carbon isotopic ratio $^{12}\text{C}/^{13}\text{C}$. The simplex algorithm (Brandt 1998) was used for χ^2 minimization in the space of 9 free parameters: 7 for abundances of C, N, O, Sc, Ti, Fe, and Ni, and 2 for rotational velocities from the H - and K -band region spectra. In most cases, when the K_r -band spectra were available there we performed additional fits to this spectral region with abundances of carbon isotopes ^{12}C and ^{13}C , and rotational velocity as free parameters. The above procedure was repeated for each target to choose the model with the best-matching metallicity. The final abundances derived on the scale of $\log \varepsilon(X) = \log(N(X)N(H)^{-1}) + 12.0$, are summarized in Table 4 together with the ratio of carbon isotopes, $^{12}\text{C}/^{13}\text{C}$, and corresponding uncertainties. The observed spectra contain some artifacts – the lines that have no counterparts in the line lists or in the synthetic spectrum that have bad data for atomic transitions. Suitable masks were prepared to exclude these lines from the analysis. Synthetic fits to the observed spectra of EG And are shown in Figs 1–3 and visualizations of the fits to all the observed spectra are available in the online Appendix C.

Our formal fitting errors were typically several hundredths of dex but up to nearly ~ 0.2 dex in a few cases of abundance values for

Ti, Sc, and Ni. Nevertheless, the actual uncertainties of the chemical composition are higher and come mainly from uncertainties in stellar parameters, to which we assign uncertainties of ~ 100 K in effective temperature, 0.5 dex in $\log g$, and ~ 0.25 km s⁻¹ in the case of ξ_t . To examine how significantly this reflects in the accuracy of determining abundances we executed additional calculations, varying the atmospheric parameters by these values. The resulting values are shown in Table B3 in the online Appendix B.

In the case of AG Peg we found an additional source of error in the measured abundances. An additional component is present in the line profiles, clearly visible in the isolated and not significantly blended, strong titanium and scandium lines in the K -band region (Fig. 4). The presence of this additional component can be seen also in the residuals of the observed and the synthetic spectra of the H - and K_r -band regions (see Figs C27 and C29 in the Appendix C), but line blending is too strong for reliable measurements. We measured the positions of these spectral features in the K -band region and compared them to the laboratory wavelengths, to obtain the radial velocities of the components. The obtained values can be found in Table 5. The radial velocity of the main component (the RG) is $V_{\text{Rad}}(A) = -19.6 \pm 1.1$ km s⁻¹. The additional, secondary component is shifted in relation to this stellar by $\text{Shift}(B) = -17.7 \pm 1.1$ towards the blue, which corresponds to its radial velocity $V_{\text{Rad}}(B) = -37.3 \pm 2.2$ km/s. We measured the equivalent widths (EW) of both components (Table 5) from the originally observed spectrum ($\text{EW}_O(A)$ and $\text{EW}_O(B)$) as well as from the synthetic spectrum ($\text{EW}_S(A)$) and from the residuals ($\text{EW}_S(B)$). Using these values we estimated that the abundances derived for AG Peg can be overestimated (i.e., in reality, they should be smaller) as a result of contribution from the secondary component to the measured profiles by ~ 0.02 dex. However, this value is smaller than the formal errors of fit (see Table 4).

A few of our targets have previously measured abundances. For CH Cyg Schmidt et al. (2006) employed wide ranges of the H and K -band regions. The resulting values agree with the current ones (derived only from the short H -band spectrum) within the error borders. EG And and AX Per have counterparts within 1 arcsec with their J2000 coordinates in the data base of Apache Point Observatory Galactic Evolution Experiment (*APOGEE*; Majewski et al. 2017; Jönsson et al. 2020). The abundances agree with our estimates with exception of nitrogen – where *APOGEE* values are lower by ~ 0.3 dex.

5 CONCLUDING DISCUSSION

We have derived here the ‘photospheric’ chemical abundances (C, N, O and elements around the iron peak: Sc, Ti, Fe, and Ni) for a sample of 14 RGs in the classical S-type SySt. They are located in the northern hemisphere with the one exception of FG Ser which is located almost exactly at the celestial equator. While the southern sample (Galan et al. 2016, 2017) is dominated by objects concentrated around the Galactic centre, the northern sample is dominated by the Galactic disc and halo (Fig. 5) and will make a useful complement to the southern sample in our ongoing comprehensive analyses of the kinematics and chemical evolution of SySt in the Galactic populations (Galan et al. – in preparation).

Metallicity is one of the most important parameters in the study of evolution in Galactic stellar populations as well as the history of interactions in binary systems, as the metallicity impacts the efficiency of the mass loss from evolved giant components, and thus on the rate of the mass exchange. As an indicator of metallicity, we use the abundance of iron that is often treated as its proxy. The distribution of the number of objects as a function of $[\text{Fe}/\text{H}]$ is shown in Fig. 6.

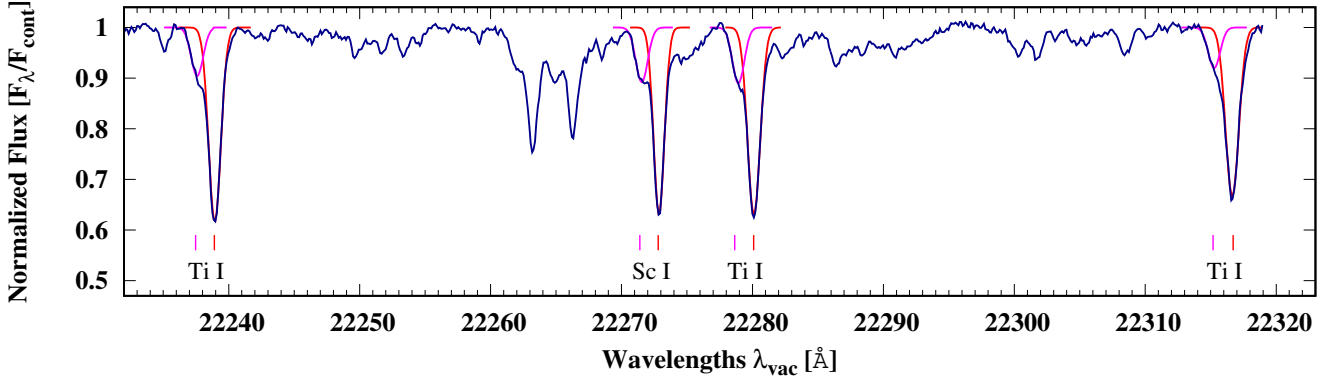


Figure 4. The spectrum of AG Peg in *K*-band region (blue line). The components of the spectral line profiles of 4 isolated, minimally blended spectral features from Ti and Sc (Table 5) are marked with red Gaussians for the stellar component originating from the RG, and with a magenta line for the additional, blue-shifted component, which must be a manifestation of some kind of interactions in the system (see the text for the details).

Table 4. The final abundances derived on the scale of $\log \epsilon(X) = \log(N(X)N(H)^{-1}) + 12.0$, relative to the Solar abundances, carbon $^{12}\text{C}/^{13}\text{C}$ isotopic ratio, and uncertainties^a.

	C	N	O	Sc ^b	Ti	Fe	Ni	$^{12}\text{C}/^{13}\text{C}$
	$\log \epsilon(X)$							
	$[X]^c$							
EG And	7.70 ± 0.03	7.81 ± 0.04	8.37 ± 0.01	3.34 ± 0.05	4.80 ± 0.04	6.93 ± 0.01	5.90 ± 0.07	7.0 ± 0.3
	-0.73 ± 0.08	-0.02 ± 0.09	-0.32 ± 0.06	$+0.18 \pm 0.09$	-0.13 ± 0.08	-0.54 ± 0.05	-0.30 ± 0.11	
AX Per	7.84 ± 0.01	8.05 ± 0.03	8.41 ± 0.02	3.87 ± 0.07	5.04 ± 0.06	7.21 ± 0.06	6.26 ± 0.06	9.5 ± 0.3
	-0.59 ± 0.06	$+0.22 \pm 0.08$	-0.28 ± 0.07	$+0.71 \pm 0.11$	$+0.11 \pm 0.10$	-0.26 ± 0.10	$+0.06 \pm 0.10$	
T CrB	8.40 ± 0.02	8.65 ± 0.04	8.79 ± 0.01	...	5.12 ± 0.09	7.82 ± 0.04	6.57 ± 0.06	...
	-0.03 ± 0.07	$+0.82 \pm 0.09$	$+0.10 \pm 0.06$...	$+0.19 \pm 0.13$	$+0.35 \pm 0.08$	$+0.37 \pm 0.10$	
FG Ser	8.08 ± 0.01	7.83 ± 0.03	8.52 ± 0.01	...	4.79 ± 0.06	7.39 ± 0.02	6.23 ± 0.05	...
	-0.35 ± 0.06	0.00 ± 0.08	-0.17 ± 0.06	...	-0.14 ± 0.10	-0.08 ± 0.06	$+0.03 \pm 0.09$	
V443 Her	8.18 ± 0.02	8.07 ± 0.03	8.62 ± 0.01	...	4.97 ± 0.10	7.45 ± 0.04	6.29 ± 0.05	...
	-0.25 ± 0.07	$+0.24 \pm 0.08$	-0.07 ± 0.06	...	$+0.04 \pm 0.14$	-0.02 ± 0.08	$+0.09 \pm 0.09$	
V1413 Aql	8.10 ± 0.05	7.74 ± 0.10	8.31 ± 0.03	...	4.45 ± 0.14	7.35 ± 0.07	6.35 ± 0.12	...
	-0.33 ± 0.10	-0.09 ± 0.15	-0.38 ± 0.08	...	-0.48 ± 0.18	-0.12 ± 0.11	$+0.15 \pm 0.16$	
BF Cyg	7.87 ± 0.03	8.23 ± 0.08	8.52 ± 0.01	3.89 ± 0.15	4.89 ± 0.10	7.22 ± 0.03	6.02 ± 0.06	6.1 ± 0.5
	-0.56 ± 0.08	$+0.40 \pm 0.13$	-0.17 ± 0.06	$+0.73 \pm 0.19$	-0.04 ± 0.14	-0.25 ± 0.07	-0.18 ± 0.10	
CH Cyg	8.26 ± 0.01	8.20 ± 0.02	8.66 ± 0.01	...	5.06 ± 0.08	7.60 ± 0.05	6.39 ± 0.07	...
	-0.17 ± 0.06	$+0.37 \pm 0.07$	-0.03 ± 0.06	...	$+0.13 \pm 0.12$	$+0.13 \pm 0.09$	$+0.19 \pm 0.11$	
QW Sge	8.30 ± 0.03	8.20 ± 0.07	8.67 ± 0.02	4.25 ± 0.12	5.28 ± 0.09	7.57 ± 0.10	6.54 ± 0.10	13.9 ± 0.8
	-0.13 ± 0.08	$+0.37 \pm 0.12$	-0.02 ± 0.07	$+1.09 \pm 0.16$	$+0.35 \pm 0.13$	$+0.10 \pm 0.14$	$+0.34 \pm 0.14$	
Cl Cyg	7.97 ± 0.04	8.17 ± 0.07	8.50 ± 0.02	4.52 ± 0.14	5.25 ± 0.06	7.37 ± 0.03	6.17 ± 0.10	12.6 ± 1.1
	-0.46 ± 0.09	$+0.34 \pm 0.12$	-0.19 ± 0.07	$+1.36 \pm 0.18$	$+0.32 \pm 0.10$	-0.10 ± 0.07	-0.03 ± 0.14	
PU Vul	8.00 ± 0.02	7.97 ± 0.03	8.34 ± 0.01	3.37 ± 0.09	4.35 ± 0.06	7.10 ± 0.02	5.90 ± 0.09	16.2 ± 0.8
	-0.43 ± 0.07	$+0.14 \pm 0.08$	-0.35 ± 0.06	$+0.21 \pm 0.13$	-0.58 ± 0.10	-0.37 ± 0.06	-0.30 ± 0.13	
V1329 Cyg	8.45 ± 0.03	8.27 ± 0.07	8.66 ± 0.02	4.36 ± 0.08	5.09 ± 0.06	7.59 ± 0.05	6.35 ± 0.06	24.0 ± 1.5
	$+0.02 \pm 0.08$	$+0.44 \pm 0.12$	-0.03 ± 0.07	$+1.20 \pm 0.12$	$+0.16 \pm 0.10$	$+0.12 \pm 0.09$	$+0.15 \pm 0.10$	
AG Peg	7.62 ± 0.03	7.82 ± 0.06	8.18 ± 0.02	3.60 ± 0.04	4.61 ± 0.05	6.96 ± 0.02	5.81 ± 0.03	5.2 ± 0.1
	-0.81 ± 0.08	-0.01 ± 0.11	-0.51 ± 0.07	$+0.44 \pm 0.08$	-0.32 ± 0.09	-0.51 ± 0.06	-0.39 ± 0.07	
Z And	8.11 ± 0.03	8.17 ± 0.06	8.56 ± 0.02	4.13 ± 0.12	5.01 ± 0.11	7.41 ± 0.04	6.33 ± 0.11	10.5 ± 0.9
	-0.32 ± 0.08	$+0.34 \pm 0.11$	-0.13 ± 0.07	$+0.97 \pm 0.16$	$+0.08 \pm 0.15$	-0.06 ± 0.08	$+0.13 \pm 0.15$	
Sun	8.43 ± 0.05	7.83 ± 0.05	8.69 ± 0.05	3.16 ± 0.04	4.93 ± 0.04	7.47 ± 0.04	6.20 ± 0.04	

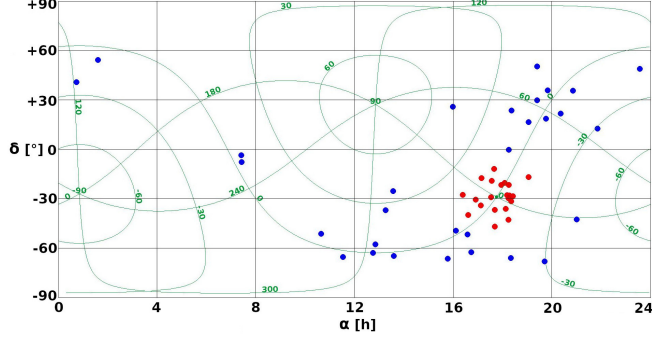
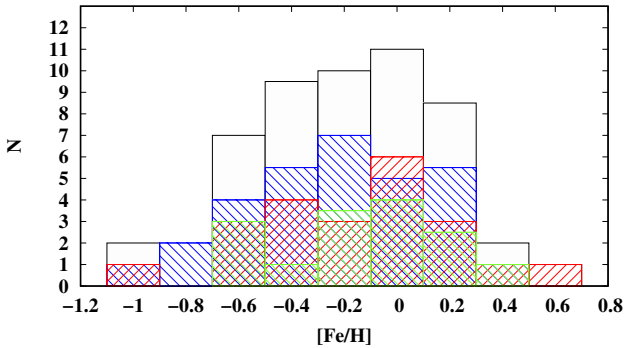
^a 3σ .

^b The abundance of scandium is based on only one strong ScI line at $\lambda \sim 22\,272.8\text{ \AA}$ and it may be less reliable than other abundances. Broadening of the IR scandium lines by hyperfine structure has not been included in the analysis (see Mikolajewska et al. 2014).

^c Relative to the Sun $[X]$ abundances in respect to the solar composition of Asplund et al. (2009) and Scott et al. (2015).

Table 5. The measured radial velocities and EWs of the components of the spectral line profiles in the *K*-band spectrum of AG Peg.

Line	$\lambda_{\text{Lab. (vac)}}$ [Å]	$\lambda_{\text{Lab. (air)}}$ [Å]	$\lambda_{\text{Meas. (air)}}$ [Å]	V_{Rad} (A) [km/s]	Shift (B) [km/s]	EW_{O} (A) [mÅ]	EW_{O} (B) [mÅ]	EW_{S} (A) [mÅ]	EW_{S} (B) [mÅ]
Ti 1	22238.90	22232.84	22231.40	-19.42	-18.07	448.6	111.8	467.2	98.0
Sc 1	22272.81	22266.73	22265.32	-18.99	-18.58	403.5	110.7	451.7	105.6
Ti 1	22280.11	22274.01	22272.57	-19.38	-16.96	432.3	111.8	473.7	106.5
Ti 1	22316.67	22310.62	22309.09	-20.56	-17.33	411.6	109.2	453.1	105.5


Figure 5. The position of southern (Galan et al. 2016, 2017) and northern (this work) SySt in the equatorial coordinate system representing objects from the bulge (red points) and other systems generally from the Galactic disc (blue points). A superimposed green grid presents the Galactic coordinate system.

Figure 6. The distribution for the number 'N' of objects, counted at 0.2 dex intervals, as a function of metallicity ([Fe/H]) for all symbiotic giants studied by us so far (black). The whole sample is divided into two subsamples: bulge stars (red) and other objects mostly from the Galactic disc (blue). The northern sample measured in this paper is shown with green.

The global distribution for all currently studied SySt has a maximum at a solar value $[\text{Fe}/\text{H}] = 0.0$ dex. It is somewhat asymmetrical and shifted towards sub-solar values with a median distribution at -0.2 dex. Most of the symbiotic giants are characterized by slightly sub-solar metallicity, as expected for an older disc population.

As with all previously analyzed symbiotic giants, those from the current northern sample have measured abundances of C, N, and O similar to those in single Galactic M giants with enhanced ^{14}N , depleted ^{12}C , and decreased $^{12}\text{C}/^{13}\text{C}$ (see Galan et al. 2016, 2017). The abundances of ^{14}N versus ^{12}C for the sample of all SySts which we have studied so far are shown in Fig. 7 (left), and they prove that all these objects have experienced the 1-st dredge-up. This is

also confirmed by the low $^{12}\text{C}/^{13}\text{C}$, which, however, being too low with respect to the theoretical predictions (Lü et al. 2008) suggests that the mixing resulting from the 1-st dredge-up is insufficient to explain the observed abundances of C, so some additional processes must be occurring. The phenomenon of thermohaline mixing (see eg. Charbonnel & Zahn 2007) is a likely possibility.

Lagarde et al. (2019) presented the first comparison between the synthetic populations computed with the improved Besançon Galaxy model (BGM; Lagarde et al. 2017) and the C and N abundances derived by the Gaia-ESO survey in field stars and in open and globular clusters. They showed that additional mixing has an impact on the C and N abundances as well as on $^{12}\text{C}/^{13}\text{C}$, which turned out to be an even better parameter for constraining extra mixing on the RGB, and works efficiently in lower mass and older giant stars ($M \leq 2.2 M_{\odot}$), especially at lower metallicities. Fig. 7–right shows our sample of symbiotic giants in the $^{12}\text{C}/^{13}\text{C}$ vs [C/N] plane compared to two models – the first with and the second without the thermohaline instability taken into account. Our results confirm that symbiotic giants may have gone through this phase of mixing with thermohaline instability. It seems that binary interaction has not significantly affected the evolution of symbiotic giants that are similar to normal M giants.

The ratios of the photospheric abundances O/N and C/N are shown in Fig. 8. Both our northern and southern samples show $\text{C}/\text{N} < \text{O}/\text{N}$, which compared to the theoretical values obtained by Lü et al. (2008) suggests that the cool components of our symbiotic systems are low-mass giants ($M < 2.5 M_{\odot}$) that have not yet undergone or have undergone only an inefficient 3-rd dredge-up.

Galan et al. (2017) have shown that these ratios obtained from nebular emission lines are shifted somewhat towards lower O/N and C/N ratios compared to values from 'photospheric' abundances, which may be due to pollution of the nebula by hot component outburst ejecta. This shift is shown on example of PU Vul. The photospheric abundances of PU Vul locate it among the other symbiotic giants, whereas those derived for the nebula move it towards abundances predicted for the nova ejecta indicating the WD mass of $0.6 M_{\odot}$ (Kato et al. 2012b). Since modelling of the outburst with the predictions for the nova ejecta from $0.65 M_{\odot}$ CO WD (Kovetz & Prialnik 1997), the behaviour of PU Vul in Fig. 8 indicates that its abundances are affected by the nova ejecta.

In addition to Fe providing information about metallicity, we also measured the abundances of two α elements: O and Ti. Due to the well-known fact that there are differences in the lifetimes of objects delivering these elements to the interstellar medium, they are especially useful in studying the chemical evolution of galaxies and the formation of stellar populations. The relative abundances of O and Ti in relation to Fe for our northern and southern samples of SySts are shown in Fig. 9 where they are compared with results from the APOGEE project. The data of the DR16 release (Jönsson et al. 2020) were filtered to reject the measurements with excessive uncertainty and various defects according to the criteria: we used only

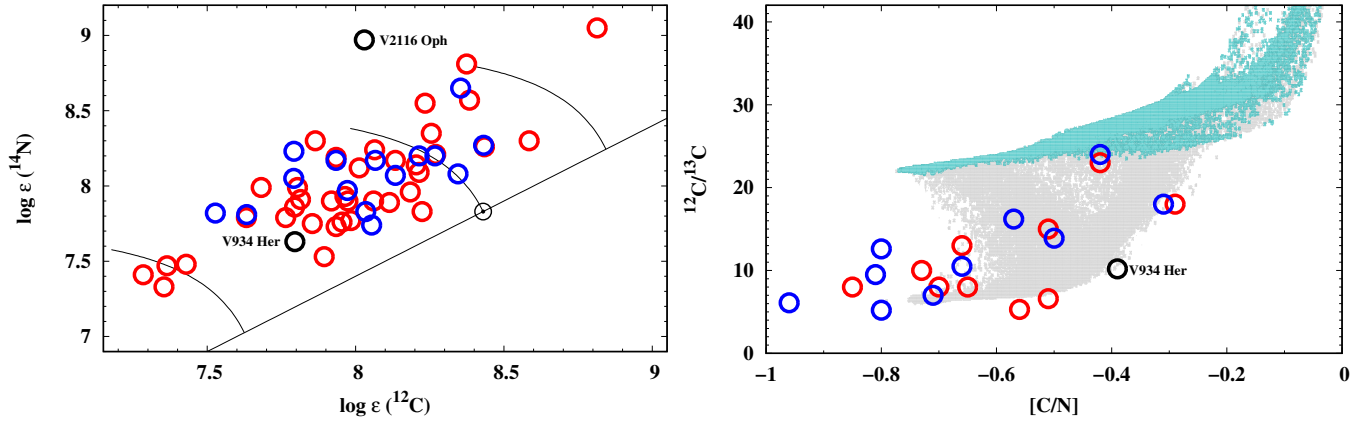


Figure 7. *Left:* Nitrogen versus carbon for the SySt from northern (blue) and southern (red) samples. Black circles mark two SySt with an accreting neutron star (V934 Her and V2116 Oph). The solid line represents scaled solar abundances, $[^{12}\text{C}/\text{Fe}] = 0$ and $[^{14}\text{N}/\text{Fe}] = 0$ whereas the solid curves delineate constant $^{12}\text{C} + ^{14}\text{N}$. *Right:* $^{12}\text{C}/^{13}\text{C}$ versus $[\text{C}/\text{N}]$ from our study compared with theoretical model predictions for synthetic populations computed with the *BGM* (Lagarde et al. 2017) with the effects of thermohaline instability (grey dots) and without (turquoise dots).

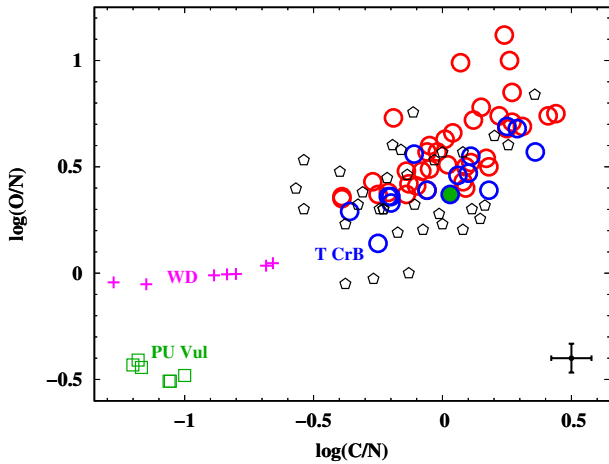


Figure 8. O/N versus C/N from the photospheric abundances. Northern (blue circles – this work) and southern (red circles – Gałan et al. 2016, 2017) samples are compared with values from nebular lines (pentagons – Nussbaumer et al. 1988; Schmid & Schild 1990; Pereira 1995; Schmid et al. 2006). The position of PU Vul from our measurements of photospheric abundances is highlighted by filling the symbol with green colour. Squares show PU Vul during outburst (Vogel et al. 1992). Crosses represent theoretical predictions for nova ejecta from CO WD with $0.65 M_{\odot}$ (Kovetz & Prialnik 1997). In the bottom-right corner is shown typical 3σ error bar.

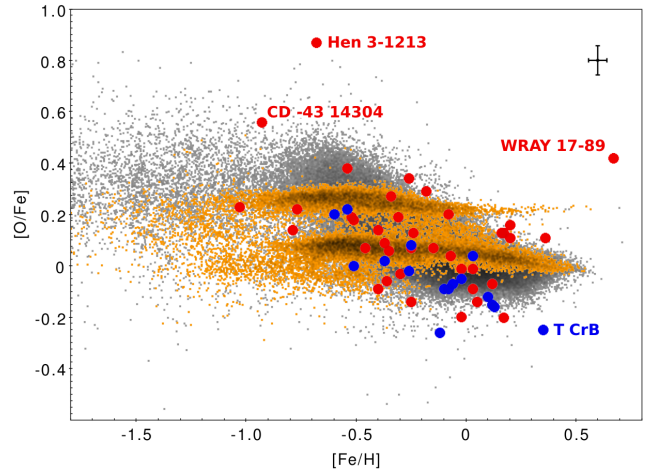


Figure 9. Oxygen relative to iron for our northern (blue circles) and southern (red circles) samples compared to the abundances coming from the entire selected sample of the *APOGEE* DR16 release (gray points) and the extracted sample of giants stars (orange points) corresponding to the atmospheric parameters ($3100 \leq T_{\text{eff}} \leq 4100$ K, and $0 \leq \log g \leq 1.5$) similar to our sample of SySt. The *APOGEE* abundances have been scaled to the solar composition by Asplund et al. (2009) and Scott et al. (2015) for oxygen and iron, respectively. Typical 3σ error bar is shown in the top-right corner.

the data from the spectra with $S/N > 70$, and all those with flags¹ *STARFLAG* and *ASPCAPFLAG* equal to zero have been rejected. Next, we removed the potential binary systems (about 6000 objects) from the sample using the following criterion: ($VSCATTER > 1$) and ($(VSCATTER/VERRMED) > 5$).

Fig. 9 shows $[\text{O}/\text{Fe}]$ vs $[\text{Fe}/\text{H}]$ diagram for whole our sample of SySt compared to *APOGEE* results for a subsample of giants characterized by atmospheric parameters (T_{eff} : 3100 – 4100 K, $\log g$: 0.0 – 1.5), similar to our sample of SySts. It is notable that this sample

of giants splits into two clearly separated ‘sequences’ which represent an α -enhanced old population and the less α -enhanced young population at lower $[\text{O}/\text{Fe}]$. Our objects coincide well with giants from *APOGEE* taking into account the uncertainty (see Tables 4 and B3) with the exception of WRAY 17-89 and Hen 3-1213. At least in some cases, discrepancies can result from an incorrect effective temperature of the giant. This can occur easily in a SySt because of the strong contribution from the nebular continuum. An example is CD-43°14304 (Gałan et al. 2017). The metallicity ($[\text{Fe}/\text{H}]$) of symbiotic giants ranges from ~ -1 to $+0.6$ dex, in most cases being consistent with membership in the disc/thick disc population, or in some cases the extended thick disc or halo.

In Fig. 10, the relative abundances of $[\text{O}/\text{Fe}]$ and $[\text{Ti}/\text{Fe}]$ versus

¹ see the web page <https://www.sdss.org/dr16/irspec/> of the *APOGEE* project with a description of how to use the data

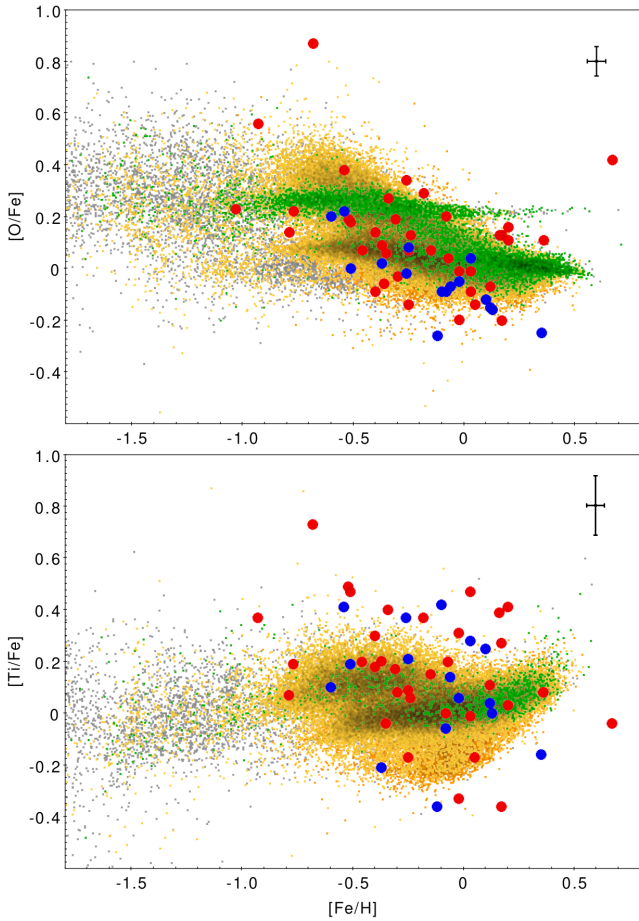


Figure 10. $[O/Fe]$ vs $[Fe/H]$ (Top) and $[Ti/Fe]$ vs $[Fe/H]$ (Bottom) for our northern (blue circles) and southern (red circles) samples, compared with various stellar populations as extracted from the *APOGEE* data: *Halo* with gray points, *Thin-* and *Thick-discs* with orange and yellow, respectively and *Bulge* with green. Thin- and Thick-discs samples percolate significantly in this representation, with the latter characterized by slightly lower $[O/Fe]$ and $[Ti/Fe]$ values and hidden under the set of points from the former. Typical 3σ error bars are shown in the top-right corners.

$[Fe/H]$ of our SySts are presented in comparison to stars from various Galactic populations. Thin- and thick-discs and halo stars have been extracted from the entire *APOGEE* dataset according to the rough criteria after Bensby et al. (2014, $V_{tot} \leq 50$ km/s, $70 \leq V_{tot} \leq 180$ km/s, and $V_{tot} > 200$ km/s, for the thin-disc, thick-disc, and halo, respectively, where $V_{tot} = (U^2 + V^2 + W^2)^{0.5}$). For the bulge stars, we adopted a very strict criterion, taking into account only objects not more than 10° from the Galactic center ($d \leq (l^2 + b^2)^{0.5}$). The populations of thin- and thick-discs and bulge permeate each other to some degree and overlap in the diagram. The positions corresponding to our SySts indicate that most of them belong to the disc or bulge populations with a few halo candidates. Nevertheless, a more detailed analysis beyond the scope of this paper, including, in particular, an exploration of the Toomre diagram, would be needed to fully explore the kinematics of these objects.

An interesting by-product of this study is radial velocities for the giant star and an additional component of the AG Peg system. We derived the RG radial velocity $V_{Rad}(A) = -19.6 \pm 1.1$ at HJD 2456904.94, which corresponds very well with the radial velocity curve by Fekel et al. (2000a). According to their final ephemeris

($Max(V) = JD\ 2446812 + 818.2 \times E$) the phase of this observation is $\phi = 0.336$, shortly before the last photometric minimum preceding the Z And type outburst that occurred in June 2015 with the light maximum between July 2-nd and 14-th (see Tomov et al. 2016) which corresponds to $\phi \approx 0.71$. The second, blue-shifted component we observed has a radial velocity $V_{Rad}(B) = -37.3 \pm 2.2$ km s $^{-1}$. This could possibly indicate a wind/an expanding circumstellar shell such as that discussed by Quiroga et al. (2002) in the case of AR Pav, and perhaps can be connected in some way with accretion on to the hot component leading to the outburst observed roughly 300 days later. Nevertheless, it should be noted that the cF absorption system in AR Pav is in antiphase with the RG while the observed radial velocity of the blue-shifted component in the case of our observation of AG Peg is evidently not. Accordingly, we cannot give a confident interpretation without additional spectroscopic data collected close in phase to this phenomenon.

ACKNOWLEDGEMENTS

This study has been supported in part by the Polish National Science Center (NCN) grant SONATA no. DEC-2015/19/D/ST9/02974 and grant OPUS no. 2017/27/B/ST9/01940. Based on observations at Kitt Peak National Observatory at NSF's NOIRLab (NOIRLab Prop. ID 2014B-0240; PI: J. Mikołajewska), which is managed by the Association of Universities for Research in Astronomy (AURA) under a cooperative agreement with the National Science Foundation. The authors are honored to be permitted to conduct astronomical research on Iolkam Du'ag (Kitt Peak), a mountain with particular significance to the Tohono O'odham. This work has made use of data from the European Space Agency (ESA) mission *Gaia* (<https://www.cosmos.esa.int/gaia>), processed by the *Gaia* Data Processing and Analysis Consortium (DPAC, <https://www.cosmos.esa.int/web/gaia/dpac/consortium>). Funding for the DPAC has been provided by national institutions, in particular the institutions participating in the *Gaia* Multilateral Agreement.

DATA AVAILABILITY

The observed Phoenix spectral images utilized in this paper are available through the Gemini Science Archive, <https://archive.gemini.edu/searchform>. The archive is searchable by object name. Reduced spectra are shown below.

REFERENCES

- Ananth, A. G., & Leahy, D. A., 1993, *JApA*, 14, 37
 Asplund, M., Grevesse, N., Sauval, A., Scott, P., 2009, *ARA&A*, 47, 481
 Bailer-Jones, C. A. L., Rybizki, J., Fouvneau, M., et al., 2018, *AJ*, 156, 58
 Belczyński, K., & Mikołajewska, J., 1998, *MNRAS*, 296, 77
 Belczyński, K., Mikołajewska, J., Munari, U., et al., 2000, *A&AS*, 146, 407
 Bensby, T., Feltzing, S., & Oey, M. S., 2014 *A&A*, 562, A71
 Bessell, M. S., & Wood, P. R., 1984, *PASP*, 96, 247
 Bessell, M. S., & Brett, J. M., 1988, *PASP*, 100, 1134
 Bessell, M. S., Castelli, F., & Plez, B., 1998, *A&A*, 333, 231.
 Boffin, H. M. J., Hillen, M., Berger, J. P., Jorissen, A., Blind, N., Le Bouquin, J. B., Mikołajewska, J., Lazareff, B., 2014, *A&A*, 564, 1
 Brandt, S., 1998, *Data Analysis, Statistical and Computational Methods*, Polish edn. Polish Scientific Publishers PWN, Warsaw
 Charbonnel, C., & Zahn, J.-P., 2007, *A&A*, 467, L15
 Chochol, D., Pribulla, T., & Tamura, S., 1998, *IBVS* No. 4571, 1

- Cúneo, V. A., Kenyon, S. J., Gómez, M. N., Chochol, D., Shugarov, S. Y., & Kolotilov, E. A., 2018, *MNRAS*, 479, 2728
- Dobrzycka, D., Kenyon, S. J., Mikołajewska, J., 1993, *AJ*, 106, 284
- Eggleton, P. P., 1983, *ApJ*, 268, 368
- Fekel, F. C., Joyce, R. R., Hinkle, K. H., & Skrutskie, M. F., 2000a, *AJ*, 119, 1375
- Fekel, F. C., Hinkle, K. H., Joyce, R. R., & Skrutskie, M. F., 2000b, *AJ*, 120, 3255
- Fekel, F. C., Hinkle, K. H., Joyce, R. R., & Skrutskie, M. F., 2001, *AJ*, 121, 2219
- Fernie, J. D., 1985, *PASP*, 97, 653
- Gaia Collaboration; Brown, A. G. A., Vallenari, A., Prusti, T., et al., 2018, *A&A*, 616, 10
- Gaia Collaboration; Brown, A. G. A., Vallenari, A., Prusti, T., et al. 2021, *A&A*, 649, 1
- Gaia Collaboration; Vallenari, A., Brown, A. G. A., Prusti, T., et al. 2023, *A&A*, 674, 1
- Gałan, C., Mikołajewska, J., Hinkle, K. H., Joyce, R. R., 2016, *MNRAS*, 455, 1282
- Gałan, C., Mikołajewska, J., Hinkle, K. H., Joyce, R. R., 2017, *MNRAS*, 466, 2194
- Glass, I. S., & Evans, T. L., 2003, *MNRAS*, 343, 67
- González-Riestra, R., Cassatella, A., & Fernández-Castro, T., 1990, *A&A*, 237, 385
- Goorvitch, D., 1994, *ApJS*, 95, 535
- Gustafsson B., Edvardsson B., Eriksson K., Jørgensen U. G., Nordlund Å., Plez B., 2008, *A&A*, 486, 951
- Hachisu, I., Kato, M., Nomoto, K., 1999, *ApJ*, 522, 487;
- Hidalgo S. L., Pietrinferni A., Cassisi S., et al., 2018 *ApJ*, 856, 125
- Hinkle K. H., Fekel F. C., Johnson D. S., & Scharlach W. W. G., 1993, *AJ*, 105, 1074
- Hinkle K. H., Cuberly R. W., & Gaughan N. A., et al., 1998, *Proc. SPIE*, 3354, 810
- Hinkle, K. H., Fekel, F. C., Joyce, R. R., 2009, *AJ*, 692, 1360
- Iijima, T., Naito, H., Nurusawa, S., 2019, *A&A*, 622, 45
- Ikeda, Y., & Tamura, S., 2000, *PASJ*, 52, 589
- Isogai, M., Seki, M., Ikeda, Y., Akitaya, H., & Kawabata, K. S., 2010, *AJ*, 140, 235
- Jarrett, T. H., Cohen, M., Masci, F. et al., 2011, *ApJ*, 735, 112.
- Jönsson, H., Holtzman, J. A., Allende Prieto, C. et al, 2020, *AJ*, 160, 120
- Joyce R., 1992, in Howell S., ed., *ASP Conf. Ser. Vol. 23, Astronomical CCD Observing and Reduction Techniques*. Astron. Soc. Pac., San Francisco, p. 258
- Jönsson, H., Holtzman, J. A., Allende Prieto, C., Cunha, K', et al., 2020, *AJ*, 160, 120
- Kato, M., Mikołajewska, J., Hachisu, I., 2012, *AJ*, 750, 5
- Kato, M., Mikołajewska, J., Hachisu, I., 2012b, *Baltic Astronomy* 21, 157
- Kenyon, S. J., 1986, *The Symbiotic Stars* (Cambridge: Cambridge Univ. Press)
- Kenyon, S. J., 1988, *AJ*, 96, 337
- Kenyon, S. J., Oliverson, N. A., Mikołajewska, J., Mikołajewski, M., Stencel, R. E., Garcia, M. R., Anderson, C. M., 1991, *AJ*, 101, 63
- Kenyon, S. J., Mikołajewska, J., Mikołajewski, M., Polidan, R. S., Slovak, M. H., 1993, *AJ*, 106, 1573
- Kenyon, S. J., & Garcia, M. R., 2016, *AJ*, 152, 1
- Kovetz A., & Prialnik D., 1997, *ApJ*, 477, 356
- Kraft, R. P., 1958, *ApJ*, 127, 625
- Kucinkas, A., Hauschildt, P. H., Ludwig, H.-G., Brott, I., Vansėvičius, V., Lindegren, L., Tanabė, T., & Allard, F., 2005, *A&A*, 442, 281
- Kupka, F., Piskunov, N., Ryabchikova, T. A., Stempels, H. C., Weiss, W. W., 1999, *A&AS*, 138, 119
- Kurucz, R. L., 1999, Available at: <http://kurucz.harvard.edu>
- Lagarde, N., Robin, A. C., Reylé, C., & Nasello, G., 2017, *A&A*, 601, 27
- Lagarde, N., Reylé, C., A. C. Robin, A. C., et al., 2019, *A&A*, 621, 24
- Lü, G., Zhu, C., Han, Z., Wang, Z., 2008, *ApJ*, 683, 990
- Liu, D., Wang, B., Ge, H., Chen, X., Han, Z., 2018, *MNRAS* 473, 5352
- Majewski, S. R., Schiavon, R. P., Frinchaboy, P. M., et al., 2017, *AJ*, 154, 94
- Mélendez, J., & Barbuy, B., 1999, *ApJS*, 124, 52
- Mikołajewska, J., & Kenyon, S. J., 1992, *AJ*, 103, 579
- Mikołajewska, J., & Kenyon, S. J., 1996, *AJ*, 112, 1659
- Mikołajewska, J., 2003, in Corradi R. L. M., Mikołajewska J., Mahoney T. J., eds, *ASP Conf. Ser. Vol. 303, Symbiotic Stars Probing Stellar Evolution*. Astron. Soc. Pac., San Francisco, p. 9
- Mikołajewska, J., Ivison, R. J., & Omont, A., 2003b, in Corradi R. L. M., Mikołajewska J., Mahoney T. J., eds, *ASP Conf. Ser. Vol. 303, Symbiotic Stars Probing Stellar Evolution*. Astron. Soc. Pac., San Francisco, p. 478
- Mikołajewska, J., Friedjung, M., & Quiroga, C., 2006, *A&A*, 460, 191
- Mikołajewska, J., Balega, Y., Hofmann, K.-H., & Weigelt, G., 2010, *MNRAS*, 403, 21
- Mikołajewska, J., 2012, *Baltic Astronomy*, 21, 5
- Mikołajewska, J., 2013, in Di Stefano, R., Orio, M., Moe, M., eds, *IAU S281, Binary Paths to Type Ia Supernovae Explosions*, Cambridge U. Press, 2013, p. 162
- Mikołajewska, J., Gałan, C., Hinkle, K. H., Gromadzki, M., Schmidt, M. R., 2014, *MNRAS*, 440, 3016
- Mikołajewska, J., & Shara, M. M., 2017, *ApJ*, 847, 99;
- Munari, U., & Jurdana-Šepić, R., 2002, *A&A*, 386, 237
- Munari, U., 2019, *Camb. Astrophys. Ser.*, 54, 77
- Mürset, U., & Schmid, H. M., 1999, *A&AS*, 137, 473
- Mürset, U., Dumm, T., Isenegger, S., Nussbaumer, H., Schild, H., Schmid, H. M., & Schmutz, W., 2000, *A&A*, 353, 952
- Nussbaumer, H., Schild, H., Schmid, H. M., & Vogel M., 1988, *A&A*, 198, 179
- Paczyński, B., 1971, *ARAA*, 9, 183
- Pereira C. B., 1995, *A&A*, 111, 471
- Phillips, J. P., 2007, *MNRAS*, 376, 1120
- Poyner, G., 2012, *JBAA*, 122, 356
- Pribulla, T., Chochol, D., & Parimucha, Š., 2003, in Corradi, R. L. M., Mikołajewska, J., Mahoney, T. J., eds, *ASP Conf. Ser. Vol. 303, Symbiotic Stars Probing Stellar Evolution*, Astron. Soc. Pac., San Francisco, p. 245,
- Price, S. D., Smith, B. J., Kuchar, T. A., Mizuno, D. R., & Kraemer, K. E., 2010, *ApJSS*, 190, 203
- Quiroga, C., Mikołajewska, J., Brandi, E., Ferrer, O., & García, L., 2002, *A&A*, 387, 139
- Richichi, A., Fabbroni, L., Ragland, S., & Scholz, M., 1999, *A&A*, 344, 511
- Schmid H. M., Schild H., 1990, *MNRAS*, 246, 84
- Schild, H., & Schmid, H. M., 1997, *A&A*, 324, 606
- Schmid, H. M., & Schild, H., 1997, *A&A*, 327, 219
- Schmidt, M. R., Začs, L., Mikołajewska, J., & Hinkle, K. H., 2006, *A&A*, 446, 603
- Schlafly, E. F., & Finkbeiner, D. P., 2011, *ApJ*, 737, 103
- Schlegel, D. J., Finkbeiner, D. P., & Davis, M., 1998, *ApJ*, 500, 525
- Scott, P., Asplund, M., Grevesse, N., Bergemann, M., Sauval, A. J., 2015, *A&A*, 573, 26
- Shugarov, S., Chochol, D., & Kolotilov, E., 2012, *Baltic Astronomy*, 21, 150
- Smith, V. V., & Lambert, D., 1988, *ApJ*, 333, 219
- Snedden, C., Lucatello, S., Ram, R. S., Brooke, J. S. A., Bernath, P., 2014, *ApJS*, 214, 26
- Stanishev, V., Zamanov, R., Tomov, N., Marziani, P., 2004, *A&A*, 415, 609
- Tatarnikova, A. A., Tatarnikov, A. M., Kolitilov, E. A., Shenavrin, V. I., Komissarova, G. V., 2018, *Astronomy Letters*, Vol. 44, No. 12, 803
- Tomov, T. V., Stoyanov, K. A., Zamanov, R. K., 2016, *MNRAS*, 462, 4435
- Van Belle, G. T., Lane, B. F., Thompson, R. R., Boden, A. F., Colavita, M. M., Dumont, P. J., Mobley, D. W., Palmer, D., Shao, M., Vasisht, G. X., Wallace, *AJ*, 117, 521
- Vogel, M., Nussbaumer, H., & Monier, R., 1992, *A&A*, 260, 156
- Wilson, R. E., & Vaccaro, T. R., 1997, *MNRAS*, 291, 54.
- Yudin, B. F., Shenavrin, V. I., Kolotilov, E. A., Tatarnikova, A. A., & Tatarnikov, A. M., 2005a, *Astron. Rep.* 49, 232
- Yudin, B. F., Kolotilov, E. A., Shenavrin, V. I., Tatarnikova, A. A., & Tatarnikov, A. M., 2005b, *A&AT*, 24, 447

APPENDIX A: NOTES ON PARTICULAR OBJECTS

A1 *EG And*

Kenyon & Garcia (2016) have refined the orbital parameters of EG And using new spectroscopic data spanning 20 years. They estimated the mass of the giant in the range $M_g = 1.1 - 2.4 M_\odot$. From observations of eclipses in the *UV* Vogel et al. (1992) derived $R_g = 74 \pm 10 R_\odot$. Wilson & Vaccaro (1997) have interpreted the *UBV* light curve variations in terms of ellipsoidal effect. By fitting light curves Kenyon & Garcia (2016) showed that the red giant is almost filling the tidal surface, and estimated its radius $R_g \sim 100-230 R_\odot$, much larger than that obtained by Vogel et al. (1992). The 2MASS (Phillips 2007) *K* magnitude is 2.58 ± 0.26 . Like other bright 2MASS sources, this measurement has a relatively large uncertainty. However, Kenyon (1988) and Ananth & Leahy (1993) obtained similar values, 2.59 ± 0.02 and 2.68 ± 0.18 , respectively. The relatively small reddening toward EG And ($E(B - V) < 0.07$) yields an intrinsic *K* magnitude ($K_0 \sim 2.60$). Adopting the Gaia's DR 3 distance 0.594 kpc we derive $R_g \sim 110 R_\odot$ (Table B1). The inclination of the orbit is not well known with literature values in the wide range $45^\circ - 90^\circ$. Here we adopt the value $i = 70^\circ$, which is compatible with the longest eclipse durations and is an upper limit from the Wilson & Vaccaro (1997) model.

A2 *AX Per*

From a comprehensive analysis of spectroscopic and photometric observations, Mikołajewska & Kenyon (1992) concluded that AX Per contains a red giant filling its Roche lobe surface and transferring the matter onto the accretion disc around its companion. They obtained the orbital solution for both components. Fekel et al. (2000b) improved the solution for the red giant by including new measurements of radial velocities and obtained a more accurate semi-amplitude for the cool component $K_g = 7.81 \pm 0.21 \text{ km s}^{-1}$ that reduced slightly the value of mass ratio to $q = 2.3 \pm 0.3$. These results indicate the mass of the RG in the system $M_g \sim 1.0 M_\odot$. For the giant filling its tidal lobe Mikołajewska & Kenyon (1992) obtained the inclination $i = 70^\circ \pm 3^\circ$. Their estimate of the giant's radius $R_g \sim 0.8 \text{ AU} = 172 R_\odot$ remains in agreement with the value obtained with the use of the Gaia parallax $R = 132^{+22}_{-22} R_\odot$ (Table B1).

A3 *TCrB*

Belczyński & Mikołajewska (1998) have analyzed ellipsoidal variations in optical light curves of T CrB together with the mass function and information on rotational velocity ($V_{\text{rot}} \sin i$) as well as taking into account evolutionary limits on the component masses to constrain the parameters of the system. They concluded that T CrB is a low mass binary system in which the giant is the less massive component ($M_g = 0.7 \pm 0.2 M_\odot$). With the mass ratio $q \approx 0.6 \pm 0.2$, the WD mass is $M_h = 1.2 \pm 0.2 M_\odot$.

Stanishev et al. (2004) have analyzed the radial velocity curves of both components including also the velocity curve of the hot component derived from the wings of H α emission, and they obtained the values: $M_g = 1.12 \pm 0.23 M_\odot$, $M_h = 1.37 \pm 0.13 M_\odot$, and the mass ratio $q \approx 0.82 \pm 0.10$. Belczyński & Mikołajewska (1998) argued that the value of $q \geq 0.8$ is unlikely because it would make the semidetached binary unstable, so we adopt here a mass ratio of approximately $q \sim 0.7$ and a resultant red giant mass close to $M_g \sim 0.9 M_\odot$. Eclipses of the hot component are not observed, and Stanishev et al. (2004) and Belczyński & Mikołajewska (1998)

both find the limit of inclination $i < 70^\circ$. Belczyński & Mikołajewska (1998) in their model adopted $i = 60 \pm 5^\circ$.

A4 *FG Ser*

The spectroscopic orbit of the cool component in FG Ser was calculated by Fekel et al. (2000b) who added the data of Mürset et al. (2000) to their set of radial velocities obtained at the Kitt Peak Observatory. The revised semi-amplitude was then $K_g = 6.92 \pm 0.26 \text{ km s}^{-1}$. In these papers the mass of the red giant was estimated as $M_g \sim 1.7 M_\odot$. Using angular diameters (0.83 ± 0.03 and $0.94 \pm 0.05 \text{ mas}$) derived from infrared interferometry by Boffin et al. (2014) and assuming the distance from the Gaia DR 3 parallax (Table B1) we estimated the stellar radius $R = 140^{+15}_{-13} R_\odot$. This value is in perfect agreement with that estimated from the parallax and infrared photometry (Table B1) and remains consistent within the cited uncertainty with $R = 105 \pm 15 R_\odot$ estimated by Mürset et al. (2000) and with the value $R \sim 116 R_\odot$ which we can obtain from the orbital period (Table 3) and rotational velocity (Table 1). Boffin et al. (2014) showed that the giant in this system is filling its Roche lobe. They were able to measure variations in angular diameter with the orbital phase which they interpreted as confirmation of ellipsoidal variations, and concluded that the inclination of the orbit should be close to being nearly edge-on. FG Ser is a known eclipsing system (Mürset et al. 2000). We adopt here $i = 90^\circ$.

A5 *V443 Her*

The spectroscopic orbit of the cool component was first analyzed by Dobrzycka et al. (1993). Fekel et al. (2000b) improved the solution including additional data from Kitt Peak Observatory. The obtained semi-amplitude is $K_g = 2.52 \pm 0.21 \text{ km s}^{-1}$, and the estimated mass of the red giant is $M_g \sim 2.5 M_\odot$. The binary is not eclipsing, which means that the inclination must be less than $\sim 60 - 70^\circ$. Dobrzycka et al. (1993) suggested $i \sim 30^\circ$ which seems to be a reasonable lower limit. The value of the red giant radius derived with the use of the Gaia DR 3 parallax and intrinsic K_0 magnitude is $R = 166 \pm 27 R_\odot$ (Table B1). Assuming synchronous rotation and taking into account the orbital period (Table 3) and the radial velocity (Table 1) would give $R \sim 120 R_\odot$.

A6 *V1413 Aql*

V1413 Aql is a symbiotic system of Z And type with an outburst observed in the 1980s and subsequent maxima in 1993 and 1995. The system remained in an active phase until May 2017 (Tatarnikova et al. 2018). There is no known spectroscopic orbit for any of the components, and we have no certain information about the parameters. We used a typical mass for symbiotic giants and the distances from Gaia DR 2, to estimate the surface gravity.

A7 *BF Cyg*

A comprehensive study of the spectroscopic orbit of the cool component in BF Cyg was made by Fekel et al. (2001). They obtained the semi-amplitude $K_g = 6.72 \pm 0.24 \text{ km s}^{-1}$. They also derived the spectroscopic orbit for the hot component using velocities measured by González-Riestra et al. (1990) from emission lines in high-resolution *IUE* spectra to obtain the semiamplitude $K_h = 24.3 \pm 4.9 \text{ km s}^{-1}$ giving a mass ratio $q = 3.6 \pm 0.9$. The resultant minimum mass of

the giant is $M_g = 1.8 \pm 0.6 M_\odot$. Yudin et al. (2005a,b) based on analysis of infrared *JK*, and *UBV* photometry obtained a stellar radius of about half the orbital semi-major axis, indicating a giant filling the Roche surface. They estimated the orbital inclination as low as $i \sim 70^\circ$, which would result in $M_g \sim 2.2 M_\odot$. Thus the red giant radius should be $R \leq 240 R_\odot$. The Gaia DR 2 parallax provides a slightly smaller radius $R_g = 163^{+40}_{-37} R_\odot$ (Table B1).

A8 CH Cyg

Hinkle et al. (2009) have refined orbital elements for the cool component of CH Cyg. They concluded that this is a binary system containing a mass accreting WD – the longest-period so far known ($P_{\text{orb}} = 5689 \pm 47$ d) in an S-type symbiotic system. They obtained the semi-amplitude $K_g = 4.45 \pm 0.12 \text{ km s}^{-1}$. Through confrontation of the stellar parameters with the stellar evolution theory, the mass of the red giant was estimated on $M_g \sim 2 M_\odot$. Analysis of the eclipse geometry yielded an estimated radius of the giant $R \sim 280 R_\odot$ and the orbital inclination $i = 84^\circ$. Iijima et al. (2019) have recently derived masses based on assumption of a triple model system hypothesis originally proposed by Hinkle et al. (1993). This model was then verified and rejected by Hinkle et al. (2009). Unfortunately, the paper by Iijima et al. does not address any of the significant caveats about this model raised in the second paper by Hinkle et al., as well as they do not provide convincing radial velocity curve for the hot component which was used to derive the masses. Thus, we do not trust these estimates.

The binary system was resolved for the first time (the components are separated by 42 ± 2 mas) by Mikołajewska et al. (2010), giving a total binary mass of about $3.7 M_\odot$, in good agreement with the mass resulting from the spectroscopic orbit derived by Hinkle et al. (2009). The distance estimated by Mikołajewska et al. (2010) 220^{+40}_{-28} pc is consistent with the new value 205^{+3}_{-4} pc derived by Gaia DR 3 (Table B1) as well as with the previous Hipparcos result 244^{+49}_{-35} pc. The 2MASS magnitudes of CH Cyg, $J = 1.07 \pm 0.29$ and $K = -0.42 \pm 0.19$ are in fairly good agreement with $J = 1.14 \pm 0.09$, $K = -0.43 \pm 0.13$ (Ananth & Leahy 1993) and $J \sim 492$ Jy, $K \sim 953$ Jy (Price et al. 2010), which when converted with the use of calibrations by Jarrett et al. (2011) and Bessell et al. (1998) give equivalent magnitudes $J \sim 1.25$ and $K \sim -0.44$, respectively. Taking into account the small reddening toward CH Cyg ($E(B - V) < 0.07$) we can estimate intrinsic K magnitude, $K_0 \sim -0.44$, and colour $(J - K)_0 \sim 1.56$. Adopting the distance provided by Mikołajewska et al. (2010) the radius of the giant is $R_g = 188 \pm 44 R_\odot$. Finally, we adopt the stellar parameters of CH Cyg ($T_{\text{eff}} = 3100 \pm 80$ and $\log g = 0.0$ – Table 2) identical to those used for abundance analysis by Schmidt et al. (2006).

A9 QW Sge

QW Sge is a very poorly studied symbiotic system with an orbital period determined from optical photometry of $P_{\text{orb}} = 390.5$ d (Munari & Jurdana-Šepić 2002). Because the orbital parameters, as well as the parameters of the system components are not known, we can only roughly estimate the mass and the radii of the giant. Therefore like in the case of V1413 Aql we used a typical mass for symbiotic giants and the distances from Gaia DR 3 together with known J and K magnitudes, to estimate the surface gravity. We adopted the value $\log g = 0.5$ (Tables 2 & B2).

A10 CI Cyg

Orbital elements of the components of CI Cyg were first studied by Kenyon et al. (1991). The spectroscopic orbit for the cool component was later refined by Fekel et al. (2000a). The orbital period ($P_{\text{orb}} = 855.25$ d) derived by Kenyon et al. (1991) from photometry remains in very good agreement with the $P_{\text{orb}} = 853.8 \pm 2.9$ d determined spectroscopically by Fekel et al. (2000a). The semi-amplitudes of radial velocity curves of both components are now well known ($K_g = 6.7 \pm 0.3 \text{ km s}^{-1}$, $K_h = 17.3 \pm 2.8 \text{ km s}^{-1}$) and they imply the mass ratio $q = 2.6 \pm 0.6$ (Mikołajewska et al. 2006). This results in the mass of the giant $M_g = 0.9 M_\odot$ if the orbit is seen edge-on ($i = 90^\circ$) and could increase up to $M_g \sim 1.27 M_\odot$ if we adopt the inclination $i = 73^\circ \pm 6^\circ$ as estimated by Kenyon et al. (1991). Using the Gaia DR 3 parallax and intrinsic K_0 magnitude we can derive the giant's radius $R = 197 \pm 37 R_\odot$ (Table B1).

A11 PU Vul

PU Vul is one of several known symbiotic novae in S-type SySt. It is an eclipsing binary with orbital period $P_{\text{orb}} \sim 4900$ d (Shugarov et al. 2012; Cúneo et al. 2018). Kato et al. (2012) used multicolour *UBVRI* light curves spanning 32 years (Shugarov et al. 2012) which covers three eclipses (in 1980, 1994, and 2007) and the archival *IUE* data to construct the composite light-curve model, and estimated the mass ($M_g = 0.8 M_\odot$), the radius ($R_g = 335 R_\odot$), and the distance to the system as $d \sim 4.7$ kpc. These values remain in pretty good agreement with $M_g = 0.76 M_\odot$ and $R_g = 282 R_\odot$ derived previously by Chochol et al. (1998). Kato et al. (2012) noted, however, that this large radius may be that of a thick TiO atmosphere, transparent in the *K*-band but opaque in the *V*-band, and the radius of the giant in the infrared can be significantly smaller. Using the bolometric luminosity – period relation for LMC Mira variables by Glass & Evans (2003) they estimated the giant luminosity ($L = 3300 L_\odot$) and radius $R_g = 187 \pm 12 R_\odot$, which we adopt as more reasonable for our considerations. The value of the Gaia DR 3 parallax together with the K_0 magnitude gives the giant's radius $R_g = 197^{+57}_{-52} R_\odot$ (Table B1).

A12 V1329 Cyg

V1329 Cyg is another symbiotic nova in our sample. The orbital inclination derived from spectropolarimetric observations (Schild & Schmid 1997) is $i = 86^\circ \pm 2^\circ$. From the analysis of the light minima, they obtained an orbital period $P_{\text{orb}} = 956.5$ d. The spectroscopic orbit solution (Fekel et al. 2001) gives the red giant semi-amplitude, $K_g = 7.85 \pm 0.26 \text{ km s}^{-1}$. Pribulla et al. (2003) using the optical emission line profiles published by Ikeda & Tamura (2000) and the radial velocities of *UV* emission lines measured from archival *IUE* spectra derived the semi-amplitude for the hot component $K_h = 22.3 \pm 2.0 \text{ km s}^{-1}$ which combined with that of the red giant yields the mass ratio $q = 2.84 \pm 0.35$ and the masses for the components $M_g = 2.02 \pm 0.51 M_\odot$ and $M_h = 0.71 \pm 0.14 M_\odot$. Assuming synchronous rotation and $V_{\text{rot}} \sin i = 10.3 \pm 0.5 \text{ km s}^{-1}$ (Table 1) we obtain the radius $R = 195 \pm 10 R_\odot$.

A13 AG Peg

AG Peg is the third symbiotic nova in our sample. The spectroscopic orbit of the cool component was calculated by Fekel et al. (2000a) who included all previously existing radial velocity measurements in their solution. They obtained the eccentric orbit ($e = 0.110 \pm 0.039$, $\omega = 112^\circ \pm 22^\circ$) and an improved semi-amplitude

APPENDIX B: SUPPLEMENTARY TABLES.

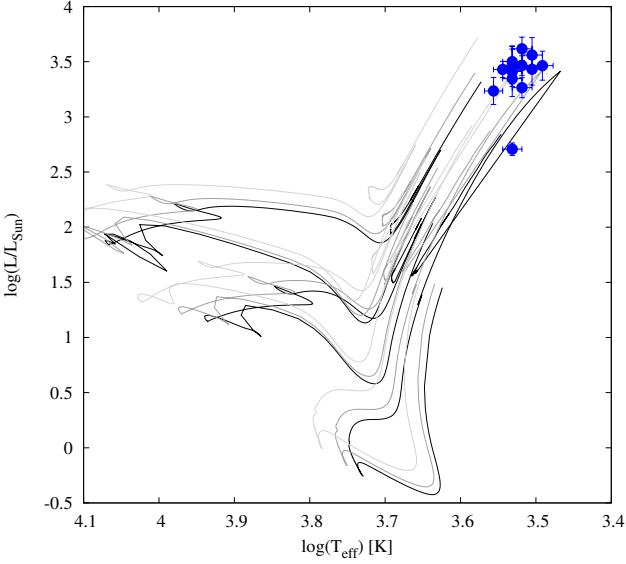


Figure A1. The H-R diagram with the positions of our targets (blue points) compared to the *BaSTI* evolutionary tracks (Hidalgo et al. 2018) for stars of mass 1, 2 and 3 M_{\odot} , and three metallicities ($Z = 0.0287$ – black, $Z = 0.0172$ (solar) – dark-gray, and $Z = 0.0077$ – light-gray).

$K_g = 5.44 \pm 0.20 \text{ km s}^{-1}$. The orbital period derived from spectroscopic data $P_{\text{orb}} = 818.2 \text{ d}$ is in very good agreement with the photometric $P_{\text{orb}} = 816.5 \text{ d}$ (Ferne 1985). Using the semi-amplitude of the hot component $K_h = 21.7 \pm 6.6 \text{ km s}^{-1}$ (Kenyon et al. 1993) yields a mass ratio of $q = 4 \pm 1.4$. Mikołajewska (2003) gives the masses of the components $M_g \geq 1.8 M_{\odot}$ and $M_h \geq 0.46 M_{\odot}$, adopting an orbital inclination $i \leq 60^\circ$. Using the angular radius ($0.50 \pm 0.02 \text{ mas}$) derived from infrared interferometry by Boffin et al. (2014) and the distance from the Gaia DR 3 parallax we estimate the stellar radius $R = 137 \pm 11 R_{\odot}$ (Table B1).

A14 ZAnd

ZAnd is a prototypical symbiotic star (Kenyon 1986). The first spectroscopic orbit of the cool component was derived by Mikołajewska & Kenyon (1996). It was refined later by Fekel et al. (2000b) who combined the radial velocity data from Mikołajewska & Kenyon (1996) with their new measurements, and obtained the semi-amplitude $K_g = 6.73 \pm 0.22 \text{ km s}^{-1}$ and the orbital period $P_{\text{orb}} = 759.0 \text{ d}$. The mass ratio is unknown but using the known mass function $f(M_g) = 0.024$ and the measured rotational velocity we can estimate its lower limit as $q \gtrsim 1.5$ –1.2. For the mass of the red giant, we adopt $M_g = 2 M_{\odot}$ (Fekel et al. 2000b). Adopting the Gaia DR 3 parallax and intrinsic K_0 magnitude we obtain the giant’s radius $R = 136^{+18}_{-19} R_{\odot}$ (Table B1). Mikołajewska & Kenyon (1996) based on analysis of optical observations suggested the range $i \sim 50^\circ - 70^\circ$. Spectropolarimetric studies of the Raman scattered O VI lines indicate $i = 47^\circ \pm 12^\circ$ (Schmid & Schild 1997) and $i = 41^\circ \pm 8^\circ$ (Isogai et al. 2010) while the continuum polarization changes suggest $i = 73^\circ \pm 14^\circ$ (Isogai et al. 2010). We choose $i = 60^\circ$ as a good compromise.

Table B1. Estimation of bolometric magnitudes and stellar radii using parallaxes from Gaia DR 3 (*Top*) (Gaia Collaboration 2023, 2021) and Gaia DR 2 (*Bottom*) (Gaia Collaboration 2018).

	ϖ [mas]	$gofAL^a$	distance [kpc]	K_0 mag	M_K mag	BC_K mag	M_{Bol} mag	R_{rg}^b [R_{\odot}]
EG And	1.645±0.034	19.3	0.594 ^{+0.014} _{-0.011}	~ 2.55	~ -6.3	~ 2.99	~ -3.3	~ 110
AX Per	0.424±0.030	12.5	2.112 ^{+0.155} _{-0.110}	5.28±0.02	-6.34±0.15	2.94±0.07	-3.41±0.23	132 ⁺²² ₋₂₂
T CrB	1.092±0.028	25.6	0.887 ^{+0.018} _{-0.029}	4.79±0.02	-4.95±0.08	2.94±0.06	-2.01±0.14	65 ⁺⁷ ₋₈
FG Ser	0.625±0.046	1.06	1.472 ^{+0.112} _{-0.090}	4.12±0.04	-6.72±0.19	2.94±0.10	-3.78±0.29	147 ⁺³¹ ₋₃₀
V443 Her	0.323±0.021	7.1	2.722 ^{+0.158} _{-0.158}	5.27±0.03	-6.90±0.15	3.00±0.07	-3.91±0.22	166 ⁺²⁷ ₋₂₇
V1413 Aql	0.069±0.030	40.4	8.817 ^{+2.162} _{-1.711}	7.27±0.02	-7.46±0.49	2.67±0.09	-4.78±0.59	234 ⁺¹¹⁵ ₋₈₇
BF Cyg	0.194±0.020	23.4	4.621 ^{+0.321} _{-0.363}	6.17±0.03	-7.15±0.19	2.97±0.07	-4.19±0.26	178 ⁺³³ ₋₃₃
CH Cyg	4.882±0.087	13.0	0.205 ^{+0.003} _{-0.004}	~ -0.44	~ -7.00	~ 3.24	~ -3.75	~ 145
QW Sge	0.202±0.027	1.10	4.852 ^{+0.576} _{-0.470}	6.73±0.03	-6.70±0.26	2.79±0.11	-3.91±0.37	156 ⁺⁴² ₋₃₈
CI Cyg	0.476±0.026	2.8	1.944 ^{+0.095} _{-0.096}	4.24±0.04	-7.20±0.15	2.91±0.12	-4.29±0.26	197 ⁺³⁷ ₋₃₇
PU Vul	0.191±0.040	38.6	4.234 ^{+0.607} _{-0.549}	6.01±0.02	-7.12±0.32	2.98±0.08	-4.15±0.40	197 ⁺⁵⁷ ₋₅₂
V1329 Cyg	0.185±0.028	18.6	4.941 ^{+0.751} _{-0.516}	6.62±0.02	-6.85±0.29	3.02±0.06	-3.83±0.36	170 ⁺⁴⁴ ₋₄₁
AG Peg	0.754±0.036	9.6	1.272 ^{+0.051} _{-0.049}	3.82±0.02	-6.70±0.11	2.88±0.08	-3.82±0.18	141 ⁺¹⁹ ₋₂₀
Z And	0.487±0.022	14.0	1.921 ^{+0.083} _{-0.075}	4.82±0.02	-6.60±0.11	2.99±0.07	-3.61±0.18	136 ⁺¹⁸ ₋₁₉
EG And	1.486±0.039	18.8	0.660 ^{+0.018} _{-0.016}	~ 2.55	~ -6.5	~ 2.99	~ -3.56	~ 120
AX Per	0.298±0.057	17.3	2.924 ^{+0.574} _{-0.423}	5.28±0.02	-7.05±0.38	2.94±0.07	-4.11±0.46	182 ⁺⁶² ₋₅₄
T CrB	1.213±0.049	31.6	0.806 ^{+0.034} _{-0.030}	4.79±0.02	-4.74±0.11	2.94±0.06	-1.81±0.17	59 ⁺⁸ ₋₈
FG Ser	0.817±0.126	24.8	1.214 ^{+0.242} _{-0.175}	4.12±0.04	-6.30±0.41	2.94±0.10	-3.37±0.51	122 ⁺⁴⁸ ₋₄₀
V443 Her	0.472±0.041	36.1	2.000 ^{+0.182} _{-0.155}	5.27±0.03	-6.24±0.21	3.00±0.07	-3.24±0.28	122 ⁺²⁴ ₋₂₄
V1413 Aql	0.140±0.038	14.8	5.557 ^{+1.432} _{-0.984}	7.27±0.02	-6.45±0.48	2.67±0.09	-3.78±0.57	147 ⁺⁷⁰ ₋₅₄
BF Cyg	0.207±0.026	6.7	4.236 ^{+0.534} _{-0.429}	6.17±0.03	-6.96±0.27	2.97±0.07	-4.00±0.34	163 ⁺⁴⁰ ₋₃₇
CH Cyg	5.464±0.217	154.8	0.183 ^{+0.007} _{-0.007}	~ -0.44	~ -6.75	~ 3.24	~ -3.51	~ 130
QW Sge	0.212±0.060	37.7	3.972 ^{+1.222} _{-0.792}	6.73±0.03	-6.27±0.56	2.79±0.11	-3.48±0.67	128 ⁺⁸² ₋₅₅
CI Cyg	0.560±0.050	26.0	1.716 ^{+0.168} _{-0.141}	4.24±0.04	-6.93±0.23	2.91±0.12	-4.02±0.35	174 ⁺⁴⁴ ₋₄₁
PU Vul	0.520±0.088	66.4	1.851 ^{+0.393} _{-0.279}	6.01±0.02	-5.33±0.41	2.98±0.08	-2.35±0.49	86 ⁺³² ₋₂₇
V1329 Cyg	0.256±0.055	36.8	3.374 ^{+0.768} _{-0.542}	6.62±0.02	-6.02±0.43	3.02±0.06	-3.00±0.50	116 ⁺⁴⁴ ₋₃₇
AG Peg	0.380±0.082	6.6	2.295 ^{+0.506} _{-0.363}	3.82±0.02	-7.98±0.42	2.88±0.08	-5.10±0.50	255 ⁺⁹⁸ ₋₈₁
Z And	0.512±0.030	17.5	1.844 ^{+0.110} _{-0.098}	4.82±0.02	-6.51±0.14	2.99±0.07	-3.52±0.21	131 ⁺²⁰ ₋₂₀

Notes. ^a $gofAL$ – the goodness-of-fit statistic parameter describing the fit quality to the data of the Gaia measurements. The better fit – the smaller its value.

^b The radii are calculated using the values of T_{eff} as listed in the penultimate column of Table 2.

Table B2. Results of estimations on surface gravities (*II*), and its limits (*I*) and (*III*) as described in the text (Section 3).

Object	log g			adopted
	(<i>I</i>)	(<i>II</i>)	(<i>III</i>)	
EG And	-0.1 <	0.4–0.7	–	0.5
AX Per	-0.1 <	0.05–0.35	< 0.3 ± 0.2	0.0
T CrB	0.4 <	~ 0.7	< 0.3 ± 0.2	0.5
FG Ser	-0.1 <	0.05–0.6	< 0.3 ± 0.4	0.5
V443 Her	-0.1 <	0.3–0.55	< 0.1 ± 0.3	0.5
V1413 Aql	–	-0.2–0.8	< 1.2 ± 0.3	0.5
BF Cyg	-0.2 <	≥ 0.0	< 0.2 ± 0.3	0.0
CH Cyg	-1.1 <	0.0–0.4	–	0.0
QW Sge	–	-0.15–0.6	< 0.8 ± 0.4	0.5
CI Cyg	-0.2 <	-0.35–0.15	< 0.4 ± 0.4	0.0
PU Vul	–	~ -0.2	< 0.2 ± 0.3	0.0
V1329 Cyg	-0.2 <	0.0–0.3	< 0.0 ± 0.2	0.0
AG Peg	-0.3 <	≥ 0.35–0.5	< 0.5 ± 0.3	0.5
Z And	-0.2 <	0.4–0.6	< 0.1 ± 0.3	0.5

Table B3. Sensitivity of abundances to uncertainties in the stellar parameters.

ΔX	$\Delta T_{eff} = +100$ K	$\Delta \log g = +0.5$	$\Delta \xi_t = +0.25$
C	+0.04	+0.21	-0.03
N	+0.03	+0.00	-0.05
O	+0.12	+0.07	-0.05
Sc	+0.13	+0.11	-0.27
Ti	+0.09	+0.12	-0.23
Fe	-0.04	+0.14	-0.07
Ni	-0.06	+0.17	-0.12

APPENDIX C: FIGURES – SPECTRA OF 15 SYMBIOTIC GIANTS OBSERVED IN K -, AND/OR K_R -, AND/OR H -BAND REGIONS, COMPARED WITH SYNTHETIC FITS.

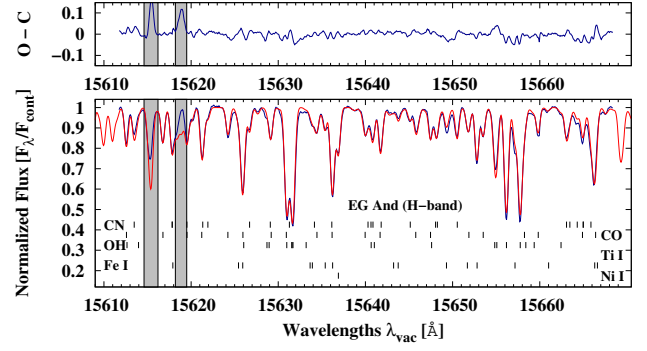


Figure C1. The H band spectrum of EG And (blue line) and a synthetic spectrum (red line) calculated using the final abundances (Table 4). The grey-shaded areas were excluded from calculations by a suitable mask.

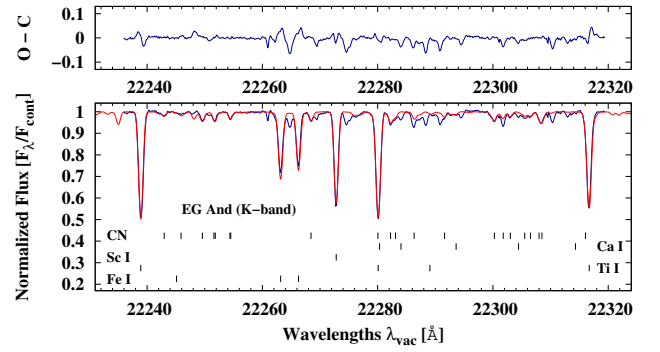


Figure C2. The K band spectrum of EG And (blue line) and a synthetic spectrum (red line) calculated using the final abundances (Table 4).

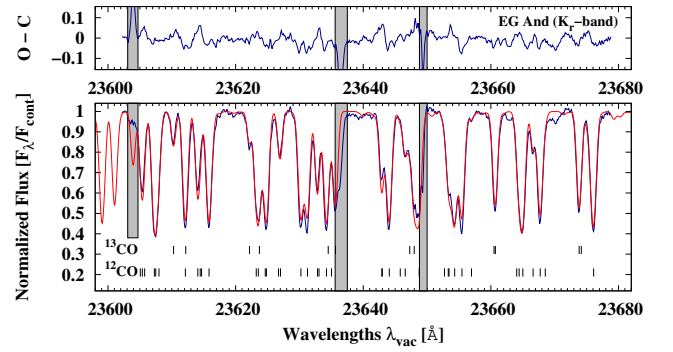


Figure C3. The K_r band spectrum of EG And (blue line) and a synthetic spectrum (red line) calculated using the final abundances (Table 4). The grey-shaded areas were excluded from calculations by a suitable mask.

This paper has been typeset from a \LaTeX file prepared by the author.

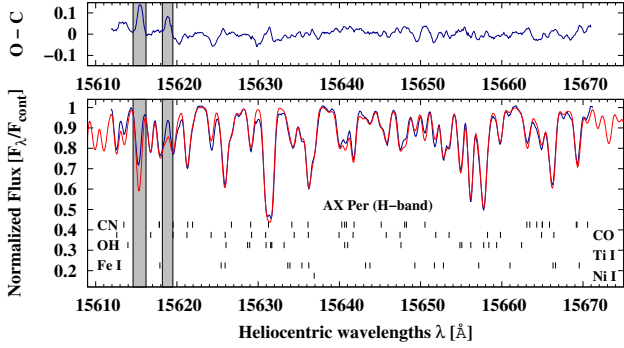


Figure C4. The H band spectrum of AX Per (blue line) and a synthetic spectrum (red line) calculated using the final abundances (Table 4). The grey-shaded areas were excluded from calculations by a suitable mask.

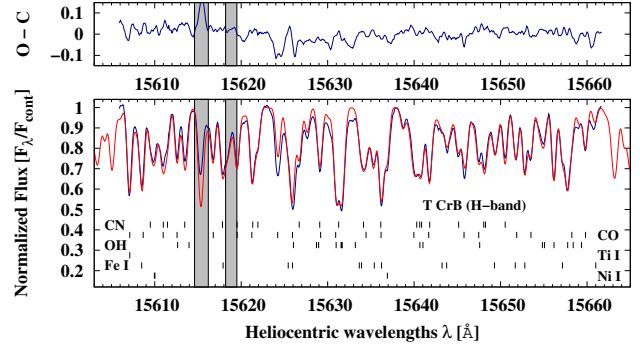


Figure C7. The H band spectrum of T CrB (blue line) and a synthetic spectrum (red line) calculated using the final abundances (Table 4). The grey-shaded areas were excluded from calculations by a suitable mask.

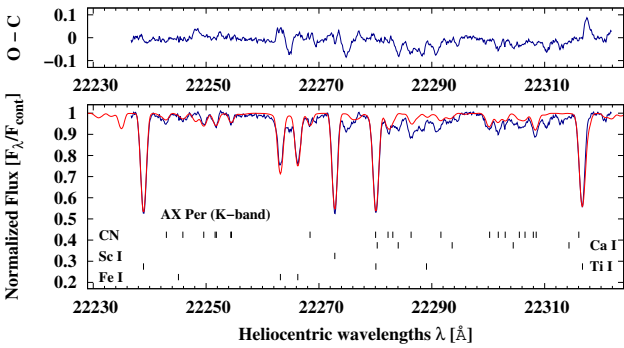


Figure C5. The K band spectrum of AX Per (blue line) and a synthetic spectrum (red line) calculated using the final abundances (Table 4).

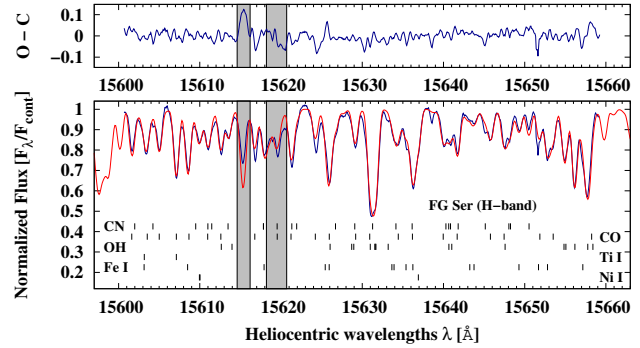


Figure C8. The H band spectrum of FG Ser (blue line) and a synthetic spectrum (red line) calculated using the final abundances (Table 4). The grey-shaded areas were excluded from calculations by a suitable mask.

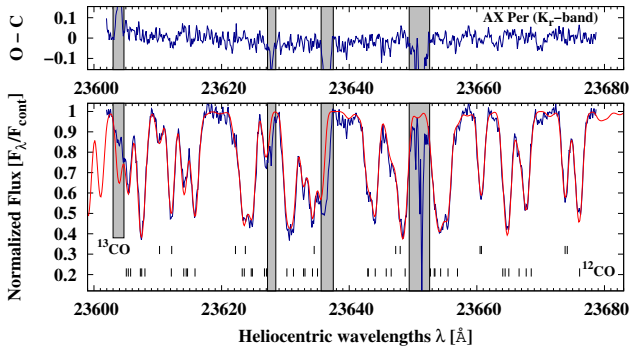


Figure C6. The K_r band spectrum of AX Per (blue line) and a synthetic spectrum (red line) calculated using the final abundances (Table 4). The grey-shaded areas were excluded from calculations by a suitable mask.

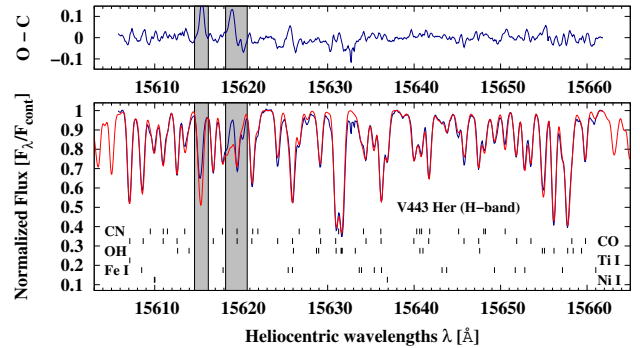


Figure C9. The H band spectrum of V443 Her (blue line) and a synthetic spectrum (red line) calculated using the final abundances (Table 4). The grey-shaded areas were excluded from calculations by a suitable mask.

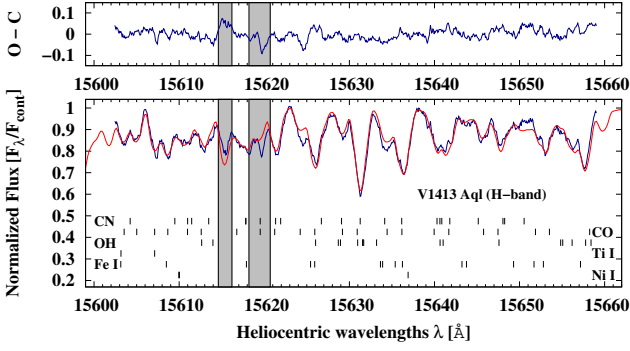


Figure C10. The H band spectrum of V1413 Aql (blue line) and a synthetic spectrum (red line) calculated using the final abundances (Table 4). The grey-shaded areas were excluded from calculations by a suitable mask.

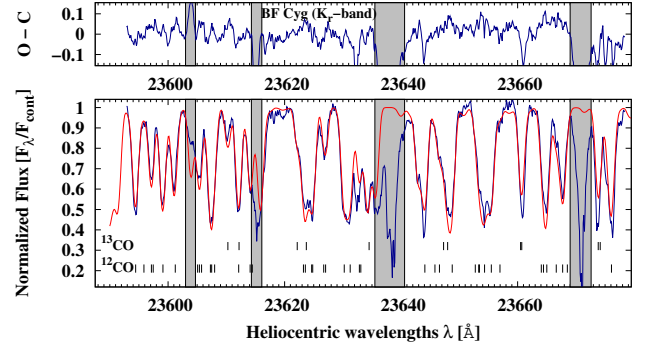


Figure C13. The K_r band spectrum of BF Cyg (blue line) and a synthetic spectrum (red line) calculated using the final abundances (Table 4). The grey-shaded areas were excluded from calculations by a suitable mask.

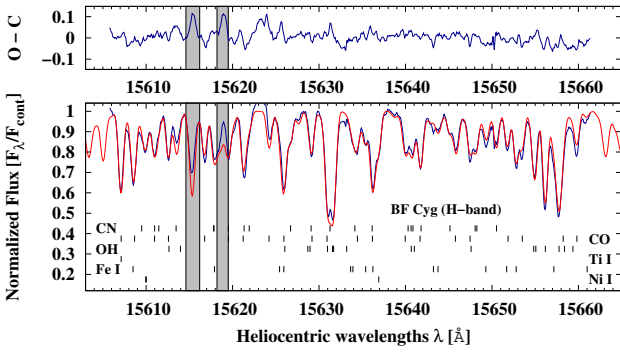


Figure C11. The H band spectrum of BF Cyg (blue line) and a synthetic spectrum (red line) calculated using the final abundances (Table 4). The grey-shaded areas were excluded from calculations by a suitable mask.

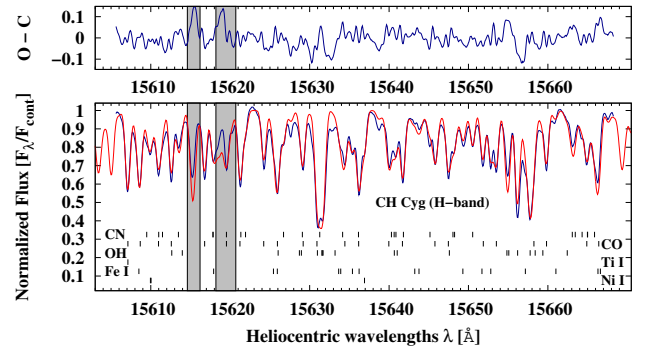


Figure C14. The H band spectrum of CH Cyg (blue line) and a synthetic spectrum (red line) calculated using the final abundances (Table 4). The grey-shaded areas were excluded from calculations by a suitable mask.

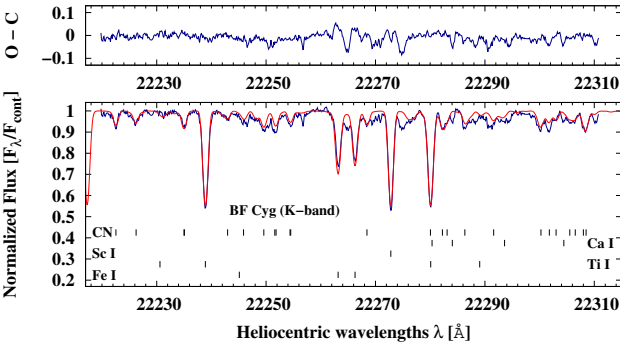


Figure C12. The K band spectrum of BF Cyg (blue line) and a synthetic spectrum (red line) calculated using the final abundances (Table 4).

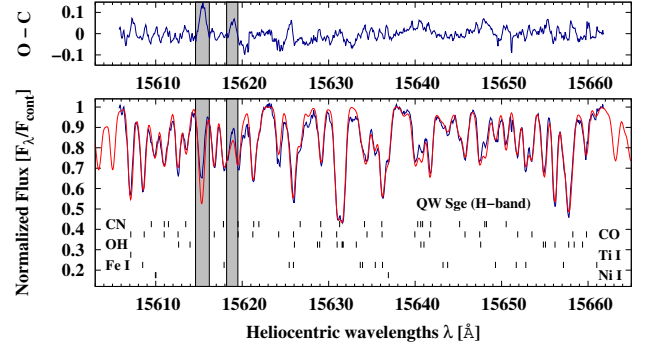


Figure C15. The H band spectrum of QW Sge (blue line) and a synthetic spectrum (red line) calculated using the final abundances (Table 4). The grey-shaded areas were excluded from calculations by a suitable mask.

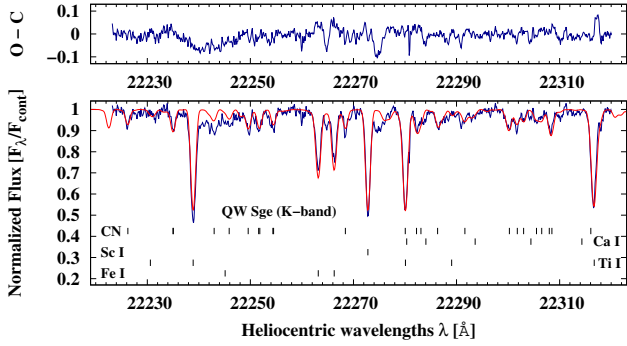


Figure C16. The K band spectrum of QW Sge (blue line) and a synthetic spectrum (red line) calculated using the final abundances (Table 4).

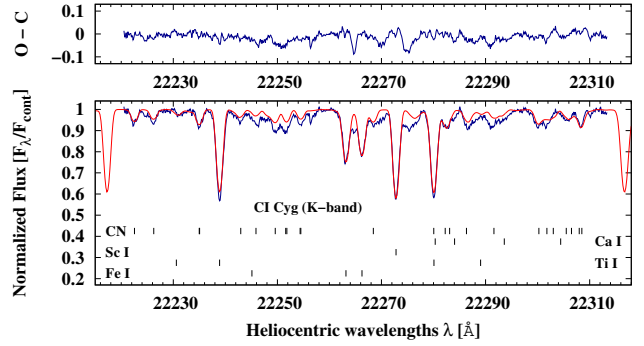


Figure C19. The K band spectrum of CI Cyg (blue line) and a synthetic spectrum (red line) calculated using the final abundances (Table 4).

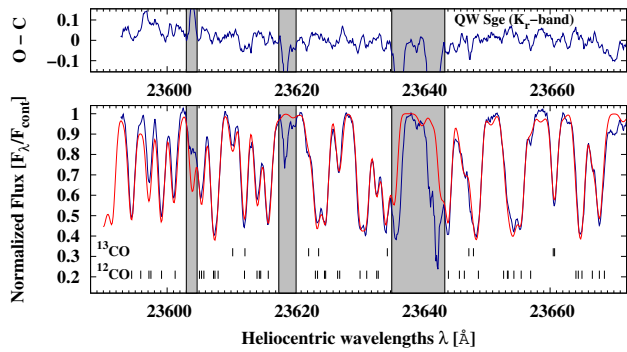


Figure C17. The K_r band spectrum of QW Sge (blue line) and a synthetic spectrum (red line) calculated using the final abundances (Table 4). The grey-shaded areas were excluded from calculations by a suitable mask.

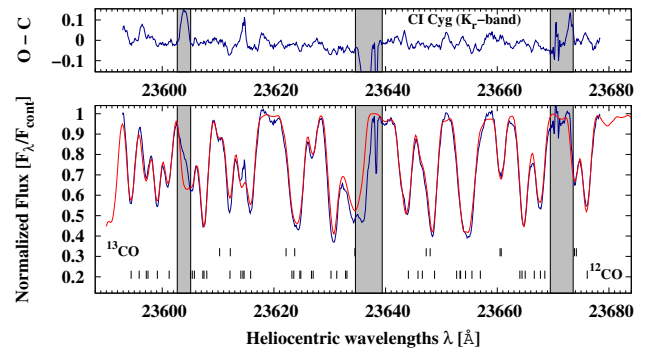


Figure C20. The K_r band spectrum of CI Cyg (blue line) and a synthetic spectrum (red line) calculated using the final abundances (Table 4). The grey-shaded areas were excluded from calculations by a suitable mask.

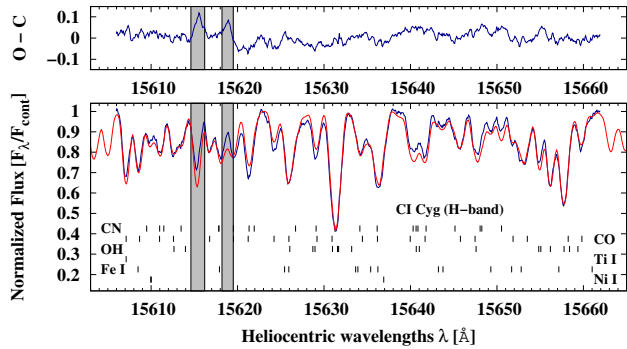


Figure C18. The H band spectrum of CI Cyg (blue line) and a synthetic spectrum (red line) calculated using the final abundances (Table 4). The grey-shaded areas were excluded from calculations by a suitable mask.

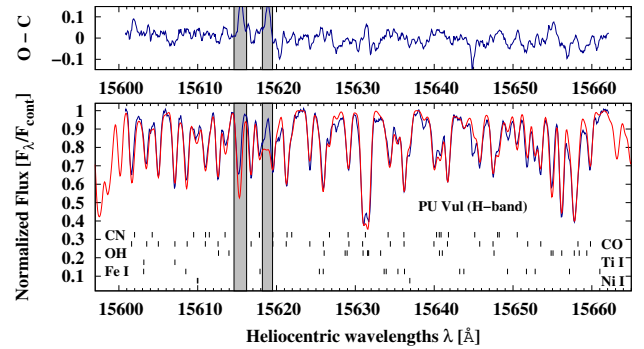


Figure C21. The H band spectrum of PU Vul (blue line) and a synthetic spectrum (red line) calculated using the final abundances (Table 4). The grey-shaded areas were excluded from calculations by a suitable mask.

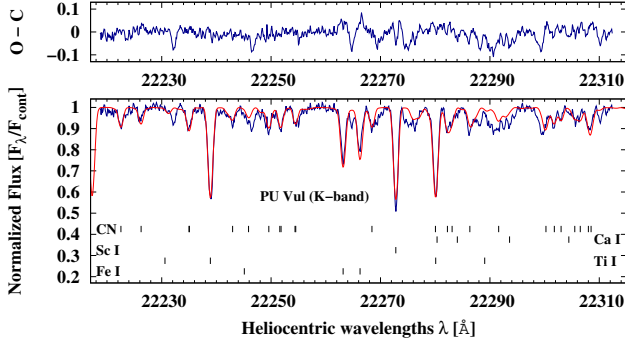


Figure C22. The K band spectrum of PU Vul (blue line) and a synthetic spectrum (red line) calculated using the final abundances (Table 4).

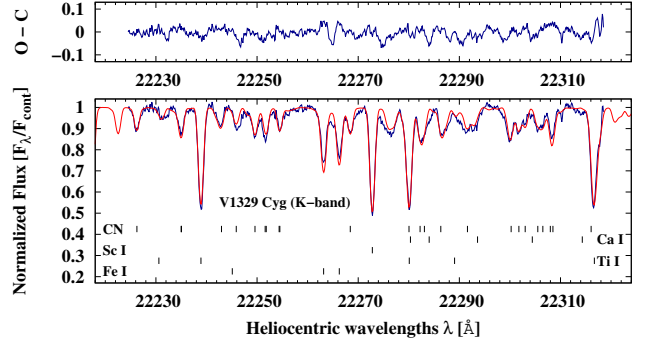


Figure C25. The K band spectrum of V1329 Cyg (blue line) and a synthetic spectrum (red line) calculated using the final abundances (Table 4).

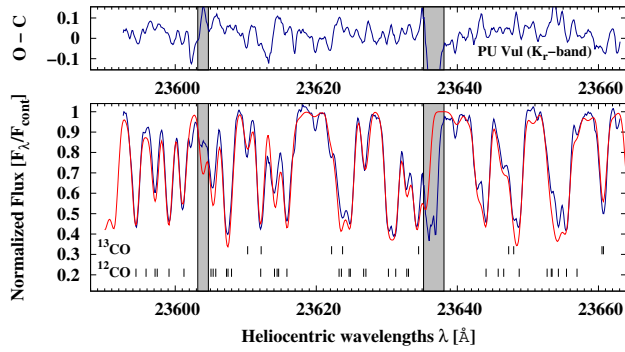


Figure C23. The K_r band spectrum of PU Vul (blue line) and a synthetic spectrum (red line) calculated using the final abundances (Table 4). The grey-shaded areas were excluded from calculations by a suitable mask.

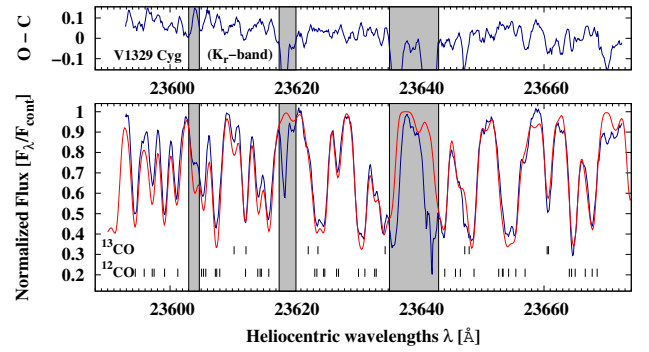


Figure C26. The K_r band spectrum of V1329 Cyg (blue line) and a synthetic spectrum (red line) calculated using the final abundances (Table 4). The grey-shaded areas were excluded from calculations by a suitable mask.

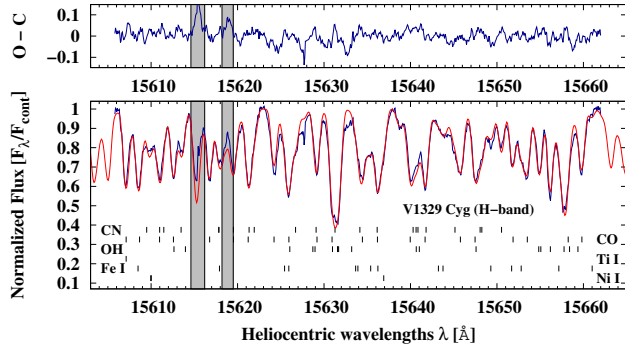


Figure C24. The H band spectrum of V1329 Cyg (blue line) and a synthetic spectrum (red line) calculated using the final abundances (Table 4). The grey-shaded areas were excluded from calculations by a suitable mask.

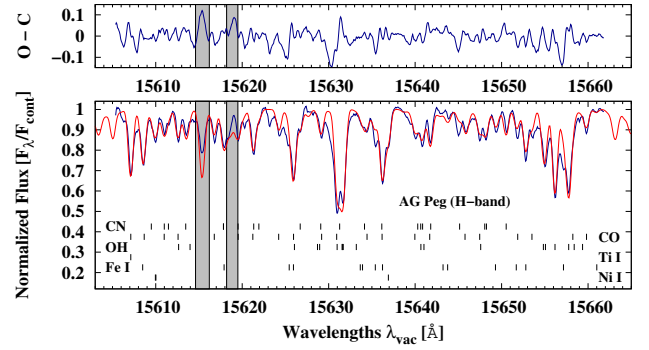


Figure C27. The H band spectrum of AG Peg (blue line) and a synthetic spectrum (red line) calculated using the final abundances (Table 4). The grey-shaded areas were excluded from calculations by a suitable mask.

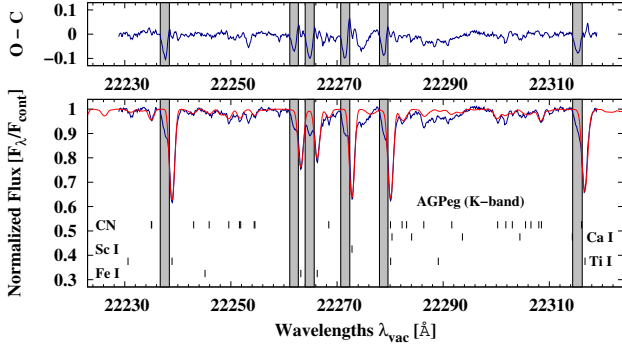


Figure C28. The K band spectrum of AG Peg (blue line) and a synthetic spectrum (red line) calculated using the final abundances (Table 4). The grey-shaded areas were excluded from calculations by a suitable mask.

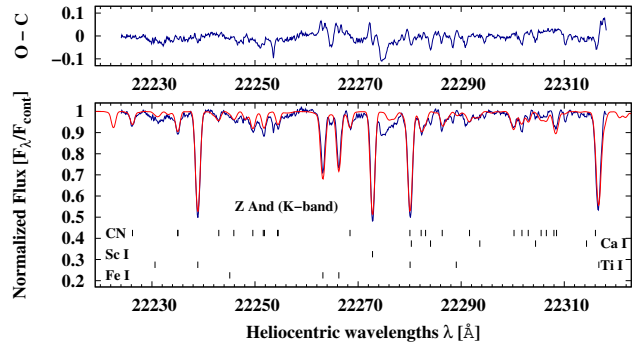


Figure C31. The K band spectrum of Z And (blue line) and a synthetic spectrum (red line) calculated using the final abundances (Table 4).

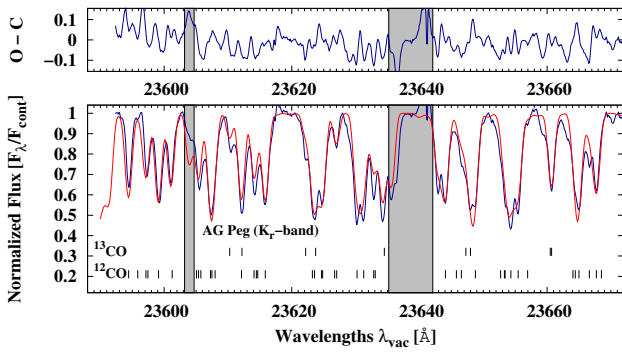


Figure C29. The K_r band spectrum of AG Peg (blue line) and a synthetic spectrum (red line) calculated using the final abundances (Table 4). The grey-shaded areas were excluded from calculations by a suitable mask.

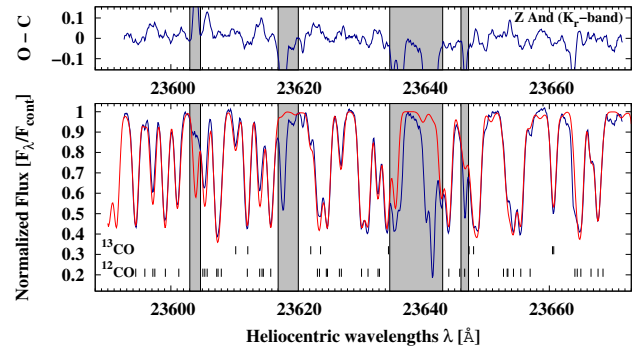


Figure C32. The K_r band spectrum of Z And (blue line) and a synthetic spectrum (red line) calculated using the final abundances (Table 4). The grey-shaded areas were excluded from calculations by a suitable mask.

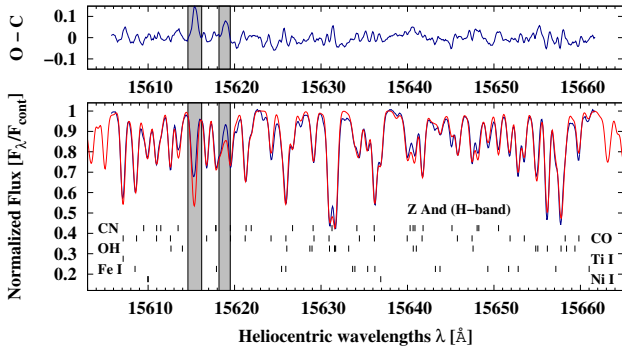


Figure C30. The H band spectrum of Z And (blue line) and a synthetic spectrum (red line) calculated using the final abundances (Table 4). The grey-shaded areas were excluded from calculations by a suitable mask.